The Electrochemical Society
Advancing solid state & electrochemical science & technology

Analysis of the Effect of Thermal Runaway Initiation Conditions on the Severity of Thermal Runaway—Numerical Simulation and Machine Learning Study

Analysis of the Effect of Thermal Runaway Initiation Conditions on the Severity of Thermal Runaway—Numerical Simulation and Machine Learning Study

Akos Kriston,[1,*,z] Andreas Podias,[2] Ibtissam Adanouj,[2] and Andreas Pfrang[2]

[1]*European Commission, Joint Research Centre (JRC), E. Fermi 2749, 21027, Ispra, Italy*
[2]*European Commission, Joint Research Centre (JRC), Westerduinweg 3, NL-1755 LE Petten, The Netherlands*

The main goal of this work is to understand the effect of thermal runaway initiation conditions on the severity of thermal runaway (TR) of Graphite—NMC (111) cells. A coupled electrical-thermal model is developed, which includes the initial energy input, the chemical decomposition processes of the anode, cathode and the electrical energy released by an internal short circuit. 780 different thermal runaway events are simulated and the output is analysed by machine learning techniques such as principal component analysis and clustering. It was found that TR events form 5 clusters between no thermal runaway and severe thermal runaway. Sensitivity analysis is applied on the 39 input invariants and the triggering energy input, resistance ratio, the heat convection coefficient, the ratio of activation energy of oxygen liberation and electrolyte evaporation are found to be the most important parameters. The later one determines the amount of electrolyte combustion. The probability of thermal runaway is calculated taking into account the most important parameters and their interactions. Finally, a combination of initiation parameters is suggested, which most likely results in a repeatable and reproducible outcome.

In various standards and regulations, safety tests[1] have been developed and are used for the characterization of safety performance of batteries during off-normal circumstances (e.g. overcharge, external short circuit, vehicle crash);[2] however assessing the safety behaviour of batteries following an internal short circuit (ISC) during normal operation[3,4] is still in the forefront of research.[5,6] The most severe effect of ISC is thermal runaway (TR), when internal heating surpasses heat dissipation and temperature increases in an uncontrolled way. As batteries in automotive and large scale storage applications consist of several hundreds of battery cells, single cell TR can spread to adjacent cells through thermal propagation (TP), which is a considerable safety risk to occupants, to buildings and to first responders. Therefore, proper safety measures need to be implemented and consequently tests need to be developed to assess the safety performance of a system in case of internal short circuit induced TP.

The first step of any TP test is the selection of a proper triggering method which is able to initiate TR on a single cell without extensive manipulation of the system and representative to manufacturing or material fault. Standards and regulations have identified several possible methods[1,7–9] but there is no common agreement which can be used for a fit-for-purpose regulation.[10] The main challenge is to initiate a chain of failure created by a local event, such as internal short circuit[11] or local heating due to e.g. chemical crosstalk,[12] which is representative for in-field failure of a cell and is controllable, repeatable and reproducible. The difficulty stems from the large number of testing (e.g. triggering method) and design parameters (e.g. chemistry, shape, size etc. of a battery system) which may potentially alter the outcome of TR and TP. Testing all possible combinations and identifying suitable control parameters requires an unmanageable number of tests. Alternatively, simulation can be used[13] to design and optimize an initiation method. However, running a validated, especially 3D model, may be prohibitively computationally expensive for assessing the effect of all combinations of possible parameters on the defined pass-fail criteria.

In this work our goal is to assess the most significant parameters of a TR initiation method (induced by internal short circuit) and to narrow down the potential testing needs. A coupled electric-thermal kinetic model is developed, which is able to mimic the dynamics of TR. Then 780 different TR events are simulated and uncertainty and sensitivity analyses are performed. The most significant parameters are identified and the probability of the different TR severities is calculated. The following questions are studied:

- What are the most influential parameters on the severity of TR?
- What is the effect of the triggering energy on TR severity?
- What are the most repeatable and reproducible testing conditions?

Thermal runaway models.—A kinetic TR model has been developed by Hatchard et al.[14] in 2001 and nowadays majority of works[12,15–18] both for the simulation of TR and TP are based on their calculations. These models are found to be accurate to predict TR occurrence,[19–21] however it may be less precise to model TR severity, because a single step kinetic for anode and cathode decomposition without interaction between the components are assumed. In our previous study[22] a new kinetic model has been developed, which takes into account multistage decomposition of anode and cathode and interaction between electrolyte evaporation, combustion and decomposition. This complex kinetic allows to model the difference in decomposition ratio between different TR events, which in turn allows the simulation of TR severity.

The natural variability of TR is rarely studied in the literature. Walker et al.[23,24] designed a special calorimeter and measured the different forms of energy release, i.e. through heat transfer and ejecta. It was concluded that the generated energy follows a lognormal distribution and the figures show large variations in the energy release. It is not clear what is the reason of this variability and if it is influenced by the initiation conditions. Therefore, in this work we take into account the standard deviation of the measured thermal triplets (activation energy, frequency factor and reaction heat) of the decomposition reactions and study the uncertainty of the outcome (i.e. TR severity) of the model results.

*Electrochemical Society Member.
zE-mail: akos.kriston@ec.europa.eu

Although different initiation techniques or abuse conditions have been studied experimentally[25–30] and by simulation,[31–34] the effect of the initiation conditions on TR severity have not been investigated thoroughly. The effect of triggering energy (i.e. heat) on the variation of severity is of utmost importance to understand since many TR initiation methods use heating to initiate TR. Heating has two major consequences: 1) it decomposes thermally unstable materials above the onset temperature and 2) it compromises the integrity of the separator (e.g. melts) which in turn creates ISC. While the thermal decomposition has been well studied in Accelerated Rate Calorimeters (ARC)[23,35] or by Differential Scanning Calorimeters (DSC)[22] the contribution of the released electrical energy from ISC to TR is not fully understood. Feng et al. suggested a time sequence diagram[36] which revealed that the heat from ISC, even though marginal, is an important factor to trigger the oxidation-reduction reactions at higher temperatures. It was also suggested[37] that if the separator collapse temperature is higher than the onset of chemical decomposition reactions ISC is not triggered and the overall heat production is smaller. Coman et al.[16] modelled the energy release from hard ISC triggered TR with an Arrhenius-type kinetic and introduced an efficiency factor. They showed that the electrical energy contributed to TR's heat production about 20%. In this work a novel approach is proposed, which models the interaction of separator breakdown and the inserted initiation energy.

Severity and sensitivity analysis.—A reproducible and repeatable test is not sensitive to small variation of testing conditions and controls all influential input parameters. In this work mathematical stability analysis based on numerical solution is applied to determine those conditions under which reproducibility and repeatability can be guaranteed.

Stability analysis of the governing equations of thermal decomposition is applied for TR by Huang et al.[38] They derived dimensionless equations for uniform (Biot number < 0.1) and non-uniform temperature distributions. It was shown that above a critical temperature and above a criticality parameter, which is a function of heat generation and heat dissipation (for any Biot number), the cell goes into TR dividing the input parameter space into two clusters (i.e. TR and NO TR). However, their model does not take into account the separator breakdown and ISC and does not further differentiate between the severity level of TR. Incorporation of ISC to the model makes the differential equations highly non-linear and so far no analytical stability analysis has been developed for the combined scenario.

For any multidimensional complex systems numerical uncertainty and sensitivity analysis can be used which have been developed[39] and used for various complex systems but not for TR. Recently, machine learning algorithms are also developed, such as K-means clustering,[40] random forest screening[40] and polynomial chaos expansion[41] to analyse such complex systems. One of the most important criteria of numerical sensitivity analysis is the generation of a random and unbiased input parameter set. Different statistical methods exists to generate points in a multidimensional space such as Latin hypercube sampling (LHS)[42] or Sobol type quasi-random low-discrepancy sequences.[39] LHS is a statistical method for generating a random sample of parameter values from a multi-dimensional distribution. The levels are spaced evenly maximizing the minimum distance between design points, and by maintaining even spacing between factor levels.

The following approach is applied in this work:

1. Development of a lumped thermal model with embedded electrical model of the cell ISC
2. Dimensional analysis of the equations and introduction of independent invariants in a semi-dimensionless form
3. Generation of a random but uniformly distributed multidimensional input space from the engineered combination of the independent invariants defining 780 different TR events by using LHS

4. Classification of TR severity clusters (uncertainty analysis) by machine learning tools
5. Sensitivity analysis and screening of the most influential input invariants
6. Calculation of the probability of the determined TR severity clusters

Mathematical Model Development

In the next sections, a lumped model is developed and invariants are defined by using dimensional analysis to reduce the dimensionality of the system. Although, the defined invariants are not dimensionless, they can be varied independently from each other within the studied range and are independent of the cell size and geometry. In this semi-dimensionless form, the results can be immediately related to real systems without losing the generality.

Energy balance.—The transient three-dimensional (3D) thermal energy conservation governs the energy transfer inside and outside the battery cell (see e.g. Abada et al.[13] and Wang et al.[43])

$$\rho_{cell} c_p \frac{\partial T}{\partial t} = \nabla \cdot (k \nabla T) + Q_{gen} \quad [1]$$

where ρ_{cell} (kg m^{-3}) is the cell density, c_p (JK^{-1} kg^{-1}) is the (mean) heat capacity of the cell, T (K) is the temperature, t (s) is time, k (Wm^{-1} K^{-1}) is the cell thermal conductivity and Q_{gen} (Wm^{-3}) is the heat generation rate per unit volume associated with reversible and irreversible heat sources (see e.g. Bernardi et al.[44]). The heat generation rate due to side reactions, that occur during abuse conditions, will be described later.

Inside the battery cell heat is conducted due to temperature gradients as $\nabla \cdot (k \nabla T)$, whereas at the cell boundary the conductive heat flux from the cell core in the n-direction ($n = x, y, z$) (left-hand side of Eq. 2 below) matches the sum of the convective and radiative heat flux. This boundary condition thus reads:

$$-k_n \frac{\partial T}{\partial n} = h_{conv}(T_{cell} - T_{amb}) + \varepsilon \cdot \sigma (T_{cell}^4 - T_{amb}^4) \quad [2]$$

where, ε, σ and h_{conv} are the emissivity (-) of the cell surface, Stefan-Boltzmann constant for radiative heat transfer (Wm^{-2} K^{-4}) and convective heat transfer coefficient (Wm^{-2} K^{-1}), respectively.

Kim[15] and Coman[16] showed that in the case of thermal runaway a lumped model with averaged heat transfer parameters gives a satisfactory match with a 3D model and is sufficient to simulate the thermal behaviour of a single cell. Surface to cell core temperature gradients are neglected and then Eqs. 1–2 combine as:

$$m_{cell} c_p \frac{dT}{dt} = Q_{gen} - A_{cell}[h_{conv}(T_{cell} - T_{amb})$$
$$+ \varepsilon \cdot \sigma (T_{cell}^4 - T_{amb}^4)] \quad [3]$$

where m_{cell} (kg) is the mass of the cell, and A_{cell}, is the cell's heat transfer area (m^2). Equation 3 is limited to homogeneous systems, when Biot number, Bi < 0.1, i.e. the variation of temperature with location within the cell body is slight and can reasonably be approximated as being uniform.[45] Furthermore, in our previous work[46] the temperature distribution resulting from a hard (external) short circuit was found to be quite uniform, therefore a lumped model is adapted in the following for modelling a coupled internal short circuit (ISC) and thermal decomposition reactions.

The main goal is to rearrange Eq. 3 and to introduce invariants which can be varied independently from each other and most importantly from the size and the format of the cell. By dividing Eq. 3 with the mass, m_{cell} and the heat capacity, c_p and substituting Q_{gen} with the chemical decomposition of the active materials, the ISC heating and the triggering energy (e.g. from a resistive heater)

we reach the following form

$$\frac{dT}{dt} = \sum_i H_i R_i + \Delta_{ISC}(I) + \Delta_{init} - \varepsilon_{conv}(T_{cell} - T_{amb})$$
$$-\varepsilon_{rad}(T_{cell}^4 - T_{amb}^4) \qquad [4]$$

where i denotes the ith component (e.g. i = anode, SEI) of the cell, and R_i is the reaction rate of decomposition of component i, which may depend on other components. $\Delta_{ISC}(I)$ is the heating rate (Ks^{-1}) caused by internal short circuit (ISC) at an electric current I (A). Δ_{ISC} is calculated from an equivalent circuit model (ECM) defined in the next subsection. Δ_{init} is the heating rate of the heater (Ks^{-1}). The chemical decomposition heat invariant (K) is

$$H_i = \frac{y_i^0 h_i}{C_p} \qquad [5]$$

where y_i^0 is the mass fraction of component i at $t = 0$ and h_i is the reaction heat (J kg^{-1}). In Eq. 5 all components are normalized by the total mass of the cell and not only by the subcomponent of a cell (e.g. anode) as it is usually applied in other papers. The corresponding reaction rates (s^{-1}) are

$$R_i = \frac{dx_i}{dt} \qquad [6]$$

where x_i (-) is the dimensionless concentration of a compound i. The details of the decomposition reactions are described later.

Introducing the density of the cell, ρ_{cell} (kg m^{-3}) the convection ε_{conv} (s^{-1}) and radiation ε_{rad} (s^{-1} K^{-3}) invariants can be expressed as follows

$$\varepsilon_{conv} = \frac{a}{C_P \rho_{cell}} h_{conv} \qquad [7]$$

and

$$\varepsilon_{rad} = \frac{a}{C_P \rho_{cell}} \varepsilon \sigma \qquad [8]$$

where $a = \frac{A_{surf}}{V_{cell}}$ is the surface-to-volume ratio of the cell (m^{-1}). The surface-to-volume ratio depends on the physical dimensions and the geometry factor of the cell.

Additionally we define $y_{NMC}^0 = \frac{\rho_{Ah}}{M_{NMC}}$, where M_{NMC} (As kg^{-1}) is the cathode active material's gravimetric capacity. $\rho_{Ah} = \frac{C_{cell}}{m_{cell}}$ is the gravimetric capacity (As kg^{-1}) of the cell where C_{cell} is the capacity of the cell (As). ρ_{Ah} is usually given for a cell technology (e.g. power or energy optimized cell) and it is considered independent from the mass and size of the cell in the studied parameter range of this work. Similar calculation can be applied to determine y_{LiC}^0.

Electrical model of internal short circuit.—Internal short circuit is approximated by an equivalent circuit model (ECM) depicted in Fig. 1. In this approach the external and internal short circuit differs only in the energy release, but not in the current potential variation. For external short circuit (ESC) the electrical energy is released outside of the cell while for ISC it is released internally, consequently heats up the cell with higher power. Since no experimental data are available for ISC current ESC tests are used to develop and validate the model.

In our previous works[30,34,46] three main time regions were identified during ESC. In region 1 the current is the highest and is governed by the resistance ratio between the cell internal and the ESC resistances. In region 2 mass transport becomes the dominant process and the current is less dependent on the resistance ratio. It was also found that the amount of discharge in region 1 is approximately 5%–10% of the total capacity of the cell regardless of the current and resistance ratio. In region 1 at very high currents the charge conservation may be not valid,[47] therefore higher current

can pass through the cell for longer time than it would be expected from the double layer capacity of the cell. In this first region, the quick/forced discharge lasts for from few 100 ms to few s and the current is inversely proportional to the resistance ratio. Region 2 is reached when the diffusion layer depletes and the charge balance is re-established at micro scale. In region 3 active materials deplete and the electromotive force (EMF) decreases leading to zero cell volt and current. It was also found in our previous ESC study[46] that TR happened in region 2 and Coman[16] found that approximately 20% of the electrical energy contributes to TR. Therefore, Region 3 is not modelled in this work, because it is assumed that TR decomposes the active materials before Region 3 is reached (i.e. full discharge). This assumption is validated in the result section also.

In this work, a simplified equivalent circuit model is suggested to simulate region 1 and 2 with the following assumptions:

- Region 1 is modelled with an apparent capacitance, which represents the double layer charge and the charge needed for redistribution of ions in the diffusion layer. This apparent capacitance is calculated to be ca. 5% of the total capacity of the cell according to the results in Ref. 46.
- Diffusion type reaction kinetic with Tafel approximation (which is valid at high overpotential) is used for charge transfer reaction
- The variation of OCV with time is negligible compared to the ohmic drop caused by the high current in Region 1 and 2 of ISC.
- The thermal decomposition of the active materials reduces SOC and terminates ISC discharge.

In order to calculate the heating rate resulting from ISC independently from the cell's size additional invariants are introduced and the ECM is solved in current rate (s^{-1}) based. We start with the introduction of the ECM and then the calculation of invariants and current rate based equations.

The total ohmic resistance of the ECM (Fig. 1) is

$$R_{Total} = R_{ISC} + R_{Int} = R_{int}(1 + y), \qquad [9]$$

where R_{ISC} and R_{int} is the internal short circuit and internal resistance (Ω), respectively. In our previous work[46] it was found that the dimensionless resistance ratio, y, can be used to describe the short circuit current for a broad range of cell sizes. The goal is to determine the short circuit current, I which can be calculated by using Kirchhoff-law

$$I = I_C + I_F = \frac{1}{R_{Total}}(V_0 - V_{OP}) \qquad [10]$$

where I, I_C and I_F is the total ISC current, capacitive current and Faradaic current (A). V_0 (V) is the electromotive force, i.e. the open circuit voltage. In this equation, the overpotential V_{OP} (V) is the unknown. By using the definition of capacitor and diffusion limited current kinetics

$$I_C = C_{AL} \frac{dV_{OP}}{dt} \qquad [11]$$
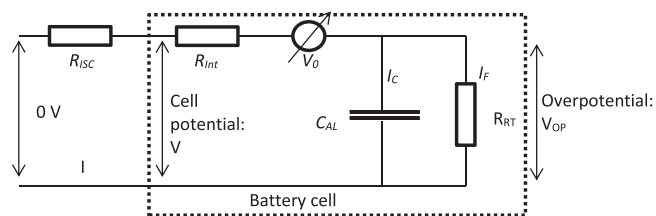
Figure 1. Simplified equivalent circuit of internal short circuit.

$$I_F = A_{AL} \frac{i_0 \exp\left(\frac{\alpha F}{RT} V_{OP}\right)}{1 + i_D \exp\left(\frac{\alpha F}{RT} V_{OP}\right)} \quad [12]$$

where C_{AL} is the apparent diffusion layer capacitance (F), i_0 is the apparent exchange current density of the cell (Am^{-2}), and A_{AL} is the total effective electrode surface area (m^2) of active material (not the geometrical surface). According to our previous work[34] i_D is a dimensionless number and can be expressed as

$$i_D = \frac{i_0 \delta}{FDc} \quad [13]$$

where δ, c, and D is the diffusion layer thickness (m), the Li-ion concentration in the active material and the diffusion rate in the diffusion layer (m^2 s^{-1}), respectively. Equations 10–12 yield the following ordinary differential equation (ODE):

$$\frac{dV_{OP}}{dt} = \frac{1}{\tau}(V_0 - V_{OP}) - i_F \quad [14]$$

where $\tau = RC_{AL}$ (s) is the relaxation time and $i_F = \frac{I_F}{C_{AL}}$ is the Faradaic current invariant.

The next step is to convert the current I (A), in Eq. 10 to current rate (s^{-1}) by normalizing the current (Eqs. 11–12) with the capacity of the cell.

In our previous experimental works[30,46] we found that in the short circuit region 1 the apparent diffusion layer capacitance depends only on the capacity of the cell and is independent of the short circuit resistance (i.e. the short circuit current). This observation can be also supported by taking into account that the thickness of diffusion layer near the material's surface depends only on the concentration,[34] consequently the amount of charge is constant. Therefore, a dimensionless diffusion layer capacitance C_{DL} can be introduced by converting Eq. 11 to current rate as follows

$$j_C = \frac{C_{AL}}{C_{Cell}} \frac{dV_{OP}}{dt} = C_{DL} \frac{dV_{OP}}{dt} \quad [15]$$

Based on our previous experimental findings C_{DL} is 5% of the total capacity; therefore it equals to 0.05.[46]

The current rate based exchange current density is

$$j_0 = i_0 \frac{A_{AL}}{C_{Cell}} = i_0 \frac{C_{Cell} m_{Ah}^{-1}}{C_{Cell}} f = i_0 \frac{P_{NMC}}{M_{NMC}} \quad [16]$$

where m_{Ah} is the active material loading (As m^{-2}) per geometrical area of the electrode, f is the roughness factor of the electrode which can be approximated by the ratio of the gravimetric surface area of the material, P_{NMC} (m^2 kg^{-1}) and the gravimetric (theoretical) capacity of the material (e.g NMC), M_{NMC} (As kg^{-1}). Therefore, the current rate based Faradaic current (s^{-1}) can be expressed as follows:

$$j_F = \frac{j_0}{C_{DL}} \frac{\exp\left(\frac{\alpha F}{RT} V_{OP}\right)}{1 + j_D \exp\left(\frac{\alpha F}{RT} V_{OP}\right)} = j_{00} \frac{\exp\left(\frac{\alpha F}{RT} V_{OP}\right)}{1 + j_D \exp\left(\frac{\alpha F}{RT} V_{OP}\right)} \quad [17]$$

where $j_D = \frac{j_{00} \delta}{FDc}$. It must be noted that to reach a simpler form of Eq. 14, C_{DL} is incorporated into invariant j_{00}.

Finally, the circuit resistance, R_{Total} needs to be converted to capacity specific values as follows.

$$R_{CR} = R_{Int} C_{cell}(1 + y) = \frac{l}{\sigma} \frac{C_{cell}}{C_{Cell} m_{Ah}^{-1}}(1 + y) = \frac{l m_{Ah}}{\sigma}(1 + y) \quad [18]$$

where l and σ are the thickness between the positive and negative current collector (m) and the effective ionic conductivity (S m^{-1}) of Li-ions in the electrolyte (assuming that the electrical conductivity is negligible), respectively.

Finally, we reach the following ODE to be solved

$$\frac{dV_{OP}}{dt} = \frac{1}{\tau}(V_0 - V_{OP}) - j_F \quad [19]$$

where $\tau = R_{CR} C_{DL}$ (s) is the relaxation time. The initial condition for the overpotential (V_{OP}) at the beginning of the ISC (until the temperature reaches T_{Init}) is

$$V_{OP}\left(t \leqslant \frac{T_{Init}}{\Delta_{Init}}\right) = 0 \quad [20]$$

After determining V_{OP} by solving the ODE Eqs. 19–20, the total short circuit current rate, $j_{CR} = j_F + j_C$ can be calculated according to Eq. 10

$$j_{CR} = \frac{1}{R_{CR}}(V_0 - V_{OP}) \quad [21]$$

Then the electrical heating rate of the discharge (Δ_{ISC} in Eq. 4) can be calculated[48]

$$j_{CR} \cdot \Gamma_{Ah}\left(V_{OP} + T \frac{\partial V_{OC}}{\partial T}\right) + (j_{CR})^2 R_{CRAh}(1 + x) \quad [22]$$

where $\frac{\partial V_{OC}}{\partial T}$ is the entropic term (VK^{-1}) of the discharge, $\Gamma_{Ah} = \frac{\rho_{Ah}}{C_p}$ (KV^{-1}) is a newly introduced invariant and j_{CR} is the total ISC current in current rate (s^{-1}).

Chemical decomposition model and its coupling to the electrical model.—In our previous work[22] a new reaction kinetic model has been developed, which takes into account a double breakdown mechanism for the lithiated graphite (LiC$_6$), multistage decomposition for de-delihiated NMC (NMC), respectively the interaction between oxygen liberation from NMC, electrolyte evaporation, combustion and decomposition. Furthermore, it is assumed that the electric discharge consumes the amount of LiC$_6$ and NMC. Therefore, the amount of material available for the decomposition reactions is linearly proportional with the discharged charge (i.e. depth of discharge, DoD). The coupling between the decomposition and the discharge can be calculated for e.g. the anode active material (LiC$_6$) by using the Faraday relationship

$$\frac{dm_{LiC_6}}{dt} = \frac{I_F}{F} Mol^{LiC_6} \quad [23]$$

where Mol^{LiC_6} is the molar mass of the material (kg mol^{-1}) and F is the Faraday constant. The initial mass of the (LiC$_6$) active electrode material can be calculated by

$$m_{LiC_6}^0 = \frac{C_{cell}}{M^{LiC_6}} \quad [24]$$

where M^{LiC_6} is the theoretical gravimetric capacity of the anode (As kg^{-1}). Dividing Eq. 23 with the initial mass of the anode active material, we reach the decomposition rate in dimensionless concentration as follows:

$$\frac{dx_{ISC}}{dt} = \frac{j_{CR}}{F} M^{LiC_6} Mol^{LiC_6} = j_{CR} \quad [25]$$

where $M^{LiC_6} Mol^{LiC_6}$ is the molar capacity of LiC$_6$ which should be equal to Faraday constant because 1 mol material contains 1 mol

charge assuming fully charged anode. j_{CR} (s^{-1}) is the solution of the ODE in Eq. 21. Assuming an ideally balanced cell it should be also equal to the cathode discharge rate.

Combining the thermal decomposition reactions determined in Ref. 22 with the ISC discharge, we reach:

Double breakdown of LiC$_6$

$$\frac{dx_{LIC}}{dt} = -A_{LIC\_II}x_{LiC}\exp\left(-\frac{E_{LIC\_II}}{k_B T}\right)$$
$$- A_{LiC\_I}x_{LiC}\exp\left(-\frac{E_{LIC\_I}}{k_B T}\right)\exp\left(-\frac{t_{SEI}}{t_{SEI,Ref}}\right) - j_{CR} \quad [26]$$

where subscript I and II refers to the first (SEI) and second breakdown of the anode, respectively.

$$\frac{dt_{SEI}}{dt} = A_{LIC\_I}x_{LIC}\exp\left(-\frac{E_{LIC\_I}}{k_B T}\right)\exp\left(-\frac{t_{SEI}}{t_{SEI,Ref}}\right) \quad [27]$$

Decomposition of anode binder and other compounds can be described by an Arrhenius-type reaction as follows:

$$\frac{dx_B}{dt} = -A_B x_B \exp\left(-\frac{E_B}{k_B T}\right) \quad [28]$$

The multistage decomposition of cathode is modelled as follows:
The first decomposition of cathode (NMC 1):

$$\frac{dx_{NMC\_I}}{dt} = -A_{NMC_I}x_{NMC_I}\exp\left(-\frac{E_{NMC_I}}{k_B T}\right) - j_{CR} \quad [29]$$

Liberation of oxygen:

$$\frac{dx_{O2}}{dt} = n_{O2}A_{NMC\_I}x_{NMC_I}\exp\left(-\frac{E_{NMC\_I}}{k_B T}\right) \quad [30]$$

where n_{O2} is the ratio of oxygen liberated from NMC.

Consumption of electrolyte by decomposition, evaporation and combustion:

$$\frac{dx_{EL}}{dt} = -A_{EL}x_{EL}\exp\left(-\frac{E_{EL}}{k_B T}\right) - A_{EVA}x_{EL}\exp\left(-\frac{E_{EVA}}{k_B T}\right)$$
$$- A_{COM}x_{EL}x_{O2}\exp\left(-\frac{E_{COM}}{k_B T}\right) \quad [31]$$

The second decomposition of cathode (decomposition of cathode binder, NMC 2):

$$\frac{dx_{NMC\_II}}{dt} = -A_{NMC\_II}x_{NMC\_II}\exp\left(-\frac{E_{NMC\_II}}{k_B T}\right) \quad [32]$$

Third decomposition of cathode (NMC 3):

$$\frac{dx_{NMC\_III}}{dt} = -A_{NMC_{III}}x_{NMC_{III}}\exp\left(-\frac{E_{NMC_{III}}}{k_B T}\right) - j_{CR} \quad [33]$$

where k_B, T are the Boltzmann constant (J K^{-1}) and the temperature (K), respectively. x_i is the corresponding dimensionless concentration $\left(\frac{y_i}{y_i^0}\right)$ of the ith compound. A_i, and E_i are frequency factor and activation energy of the *ith* reaction, respectively.

The details of all variables are listed in Table I.

Initiation of thermal runaway—energy input and separator break down.—TR can be initiated by heating the cell or by creating an ISC (by e.g. nail penetration). In practice ISC happens after a

certain energy input (i.e. heating) which melts the separator or activates an ISC device[49] Furthermore energy input is hard to stop exactly when the ISC or TR happens, i.e. energy input may continue after ISC or TR occurred. In order to analyse the effect of energy input before and after ISC on the severity of TR two parameters are introduced: 1) heater switch off temperature (T_{Heat}) and 2) separator breakdown temperature (T_{Init}) when the electrical discharge starts. All events start with heating the system with e.g. a resistive heater. During heating the cooling effect is compensated in the simulation, i.e. all heat is going into the cell (perfect heater). The heater is stopped at a predefined temperature (T_{Heat}) after that the cooling is not compensated anymore and the system behaves without any external restrictions. Thermal initiation happens when $T_{Heat} < T_{Init}$ and ISC initiation occurs when $T_{Heat} > T_{Init}$ (Fig. 2). For thermal initiation TR cannot occur when the self-heating rate is smaller than the cooling rate after the heater is switched off. Combined initiation (ISC and thermal) happens when self-heating heats up the cell's temperature, T_{TR} above T_{Heat} until T_{Init} is passed, i.e. $T_{TR} > T_{Init}$ (and there is still active material available).

In this model nail penetration occurs when T_{Init} is equal to room temperature. For any ISC device, e.g. wax method,[49] T_{Init} is higher than room temperature and $T_{Heat} > T_{Init}$. The maximum value of T_{Init} is assumed to be 400 °C to cover future more thermally stable than currently in use separator technologies. Consequently, the maximum value of T_{Heat} is 400 °C.

In all cases the energy needed to heat up the cell to reach T_{Heat} is calculated independently from the control parameters.

The heating rate is calculated from a draft regulation (UN ECE R100 v3), i.e. to reach 300 °C in 30 min, which equals to 10 °C min^{-1}.

Assumptions and limitations of the current work.—*Assumptions.*—

1. The heat that leads to thermal runaway originates from external heating, electrical discharge and exothermic decomposition reactions of the active materials and electrolyte.
2. The battery cell is composed of jellyroll consisting of active materials packed inside a casing (in a pouch cell or in a hard casing).
3. Interactions between the thermal decomposition and electric discharge is considered.
4. Interactions are considered between the components such as: combustion of electrolyte with the liberated oxygen from NMC, electrolyte evaporation and combustion, primary and secondary SEI breakdown.
5. The evaporated electrolyte vents from the battery cell and so does not take part in further reactions inside the cell (e.g. combustion). The combustion with external oxygen is not modelled in this work.
6. The battery cell temperature is uniform and any temperature gradient is neglected. The low Biot warrants the use of lumped thermal model (Bi ≪ 0.1; a Biot number of 0.0179 was reported by Hatchard et al.[14]).
7. The thermal conductivity of the heat conducting materials is isotropic and constant. The battery cell specific heat capacity assumed to be constant at any temperature.
8. The electrochemical constants (e.g. diffusion rate, electrical conduction) are independent of the concentration and constant in time.
9. ISC is constant in time.
10. The heat is dissipated to the surrounding by convective and radiative heat transfer.
11. The Joule-Thompson cooling effect instigated by venting of gases and expulsion of battery content is not considered.

Limitations.—The model is designed to assess the significance and importance of the parameters and is balanced between computational cost and model fidelity. However, the model can be applied to other problems with the following limitations:

Table I. Derived invariants and range of variation. The column "Invariant name" refers to the notation used in the simulation program and it is the same as the column names in the data files enclosed in the supplementary materials. *The diffusion coefficient has been slightly adjusted manually, resulting in an increase in diffusion limiting current from 0.4 to 0.635 to match with the experimental results in Ref. 46.

Symbol	Invariant name	Formula	Description	Dimension	Mid value	Value low	Value high	References
R_{int}	R_int	$\frac{lm_{Ah}}{\sigma}$	Internal resistance invariant	Vs	4.50×10^1	1.01×10^1	2.17×10^2	
l	—		Thickness of the electrode	m	10^{-4}	5.0×10^{-5}	2.50×10^{-4}	CustomCells[34]
σ	—		Effective ionic conductivity	S m^{-1}	0.16	0.145	0.178	[34]
m_{Ah}	—		Active material loading on unit electrode surface	As m^{-2}	7.2×10^4	3.6×10^4	1.25×10^5	[34]
c_{dl}	Cd		Dimensionless diffusion layer charge invariant	—	5.00×10^{-2}	4.50×10^{-2}	5.50×10^{-2}	[46]
j_{00}	aa	$\frac{i_0 P_{NMC}}{M_{NMC} c_{dl}}$	Exchange current density invariant (in current rate)	s^{-1}	1.04×10^{-1}	7.67×10^{-2}	1.40×10^{-2}	
i_0	—	i_0	Exchange current density per real surface area	Am^{-2}	1	0.9	1.1	[33, 34]
M_{NMC}	—	M_{NMC}	Theoretical capacity of NMC	As kg^{-1}	5.76×10^5	—	—	[34]
P_{NMC}	—	P_{NMC}	Gravimetric surface area	m^2 kg^{-1}	3×10^3	—	—	CustomCells
j_D	jd	$\frac{j_{00} \cdot \delta}{FDc}$	Dimensionless diffusion current ratio*	—	6.35×10^{-1}	3.83×10^{-1}	1.04	
δ	—		Diffusion layer thickness	m	1×10^{-7}	9.0×10^{-8}	1.1×10^{-7}	[34]
D	—		Diffusion coefficient*	m^2 s^{-1}	1.7×10^{-16}	10%		[34] adjusted
c	—		Li-ion concentration	mol m^{-3}	1000	—	—	[34]
Γ_{Ah}	Ah	$\frac{\rho_{Ah}}{c_p}$	Capacity ratio	KV^{-1}	1.45×10^2	9.86×10^2	4.82×10^2	
ρ_{Ah}	—	ρ_{Ah}	Charge density	As kg$_{cell}$$^{-1}$	1.2×10^5	9×10^4	3.6×10^5	Custom Cells
c_p	—	c_p	Heat capacity of the cell	Jkg^{-1} K^{-1}	8.3×10^2	7.47×10^2	9.13×10^2	[16]
T_{Init}	TIniT	T_{Init}	Separator breakdown temp.	K		300	700	
T_{Heat}	THeaT	T_{Heat}	Heater switch off temp.	K		300	700	
ε_{rad}	eps	$a\frac{\varepsilon\sigma}{c_p \rho_{cell}}$	Radiation efficiency	s^{-1} K^{-3}	4.71×10^{-12} E-12	8.75×10^{-14}	4.36×10^{-11}	
a			Surface to volume ratio	m^{-1}	222	40	1333	This work
ρ_{Cell}			Density of the cell	kg m^{-3}	2580	2322	2838	[16]
ε			Emissivity		0.8	0.1	1	[16]
σ			Stefan-Boltzmann constant	W m^{-2} K^{-4}	5.67×10^{-8}	—	—	—
ε_{conv}	h_conv	$a\frac{h_{conv}}{c_p \rho_{cell}}$	Convection efficiency invariant	s^{-1}	7.26×10^{-4}	1.54×10^{-5}	1.54×10^{-2}	
		h_{conv}	Convective heat transfer coefficient	W m^{-2} K^{-1}	7	1	20	[16]
A_{LIC_I}	A_LiC_I	A_{LIC_I}	Frequency factor of first breakdown of anode	s^{-1}	1.67×10^{15}	1.50×10^{15}	1.84×10^{15}	[22]
E_{LIC_I}	E_LiC_I	E_{LIC_I}	Activation energy of first breakdown of anode	J	2.24×10^{-19}	2.02×10^{-19}	2.46×10^{-19}	[22]
H_{LIC}	h_LiC_I	$\frac{y^0_{LIC} h_{LIC\_I}}{c_p}$	Heat of reaction invariant of first breakdown	K	1.51×10^2	9.24×10^1	5.52×10^2	[22]
y^0_{LIC}	—		Initial weight percent of anode	%	9.52×10^{-2}	7.14×10^{-2}	2.86×10^{-1}	This work
h_{LIC_I}	—			J kg^{-1}	1.31×10^6	1.18×10^6	1.44×10^6	[16, 22]

Table I. (Continued).

Symbol	Invariant name	Formula	Description	Dimension	Mid value	Value low	Value high	References
			Heat of reaction of first breakdown/normalized by the amount of anode					
t_{SEI}	—		Initial tunneling factor of the secondary SEI build up	—	0.05	—	—	16, 22
$t_{SIE,Ref}$	X_SEI		Tunneling reference factor of the secondary SEI build up	—	0.033	—	—	16, 22
A_{LIC_II}	A_LiC_II		Frequency factor of second breakdown	s^{-1}	1.78×10^{14}	1.26×10^{14}	2.30×10^{14}	22
E_{LIC_II}	E_LiC_II		Activation energy of second breakdown - electrolyte reaction	J	2.69×10^{19}	2.28×10^{19}	3.10×10^{19}	22
	h_LiC_II	$\frac{y_{LIC}^0 h_{LIC\_II}}{c_p}$	Heat of reaction invariant of 2nd breakdown	K	5.50×10^1	3.25×10^1	2.07×10^1	
h_{LIC_II}	—		Heat of reaction of second breakdown- LiC_6—electrolyte reaction	$J\ kg^{-1}$	4.79×10^5	4.16×10^5	5.42×10^5	22
A_{bin}	A_bin		Frequency factor Anode binder	s^{-1}	5.62×10^6	2.46×10^6	8.78×10^6	22
E_{bin}	E_bin		Activation energy Anode binder	J	1.60×10^{19}	1.03×10^{19}	2.17×10^{19}	22
H_{Bin}	h_bin	$\frac{y_{LIC}^0 h_{bin}}{c_p}$	Heat of reaction invariant of Anode binder	K	2.39×10^1	1.45×10^1	8.84×10^1	
h_{bin}	—		Heat of reaction - Anode binder	$J\ kg^{-1}$	2.08×10^5	1.85×10^5	2.31×10^5	22
A_{NMC_I}	A_1		Frequency factor NMC1	s^{-1}	3.22×10^{10}	2.29×10^{10}	4.15×10^{10}	22
A_{NMC_II}	A_2		Frequency factor NMC2	s^{-1}	3.78×10^{12}	3.48×10^{12}	4.08×10^{12}	22
A_{NMC_III}	A_3		Frequency factor NMC3	s^{-1}	1.30×10^{16}	1.10×10^{16}	1.50×10^{16}	22
E_{NMC_I}	E_1		Activation energy NMC1	J	2.35×10^{19}	2.05×10^{19}	2.65×10^{19}	22
E_{NMC_II}	E_2		Activation energy NMC2	J	3.41×10^{19}	3.28×10^{19}	3.54×10^{19}	22
E_{NMC_III}	E_3		Activation energy NMC3	J	4.80×10^{19}	4.40×10^{19}	5.20×10^{19}	22
H_{NMC_I}	h_1	$\frac{y_{NMC}^0 h_{NMC\_I}}{c_p}$	Heat of reaction invariant of NMC1 by cell weight	K	2.51×10^1	1.41×10^1	9.83×10^1	
y_{NMC}^0	—	y_{NMC}^0	Initial weight percent of NMC	%	2.08×10^{-1}	1.56×10^{-1}	6.25×10^{-1}	This work
h_{NMC_I}	—	h_{NMC_I}	Heat of reaction NMC1 by active material weight	$J\ kg^{-1}$	1.0×10^5	8.26×10^4	1.17×10^5	22
H_{NMC_II}	h_2	$\frac{y_{NMC}^0 h_{NMC\_II}}{c_p}$	Heat of reaction invariant of NMC1 by cell weight	K	5.32×10^1	3.30×10^1	1.94×10^1	
h_{NMC_II}	—	h_{NMC_II}	Heat of reaction NMC2 by active material weight	$J\ kg^{-1}$	2.12×10^5	1.93×10^5	2.31×10^5	22
H_{NMC_III}	h_3	$\frac{y_{NMC}^0 h_{NMC\_III}}{c_p}$	Heat of reaction invariant of NMC3 by cell weight	K	4.74×10^1	2.94×10^1	1.73×10^2	
h_{NMC_III}	—	h_{NMC_III}	Heat of reaction invariant of NMC3 by active material weight	$J\ kg^{-1}$	1.89×10^5	1.72×10^1	2.06×10^1	22
A_{el}	A_el	A_{el}	Frequency factor EL decomposition	s^{-1}	5.14×10^{25}	4.63×10^{25}	5.65×10^{25}	22
n_{O2}	n_o2	n_{O2}	Liberated oxygen ratio	—	0.14	—	—	22
E_{el}	E_el	E_{el}	Heat of reaction - EL decomposition	J	3.78×10^{-18}	3.40×10^{-18}	4.16×10^{-18}	22

Table I. (Continued).

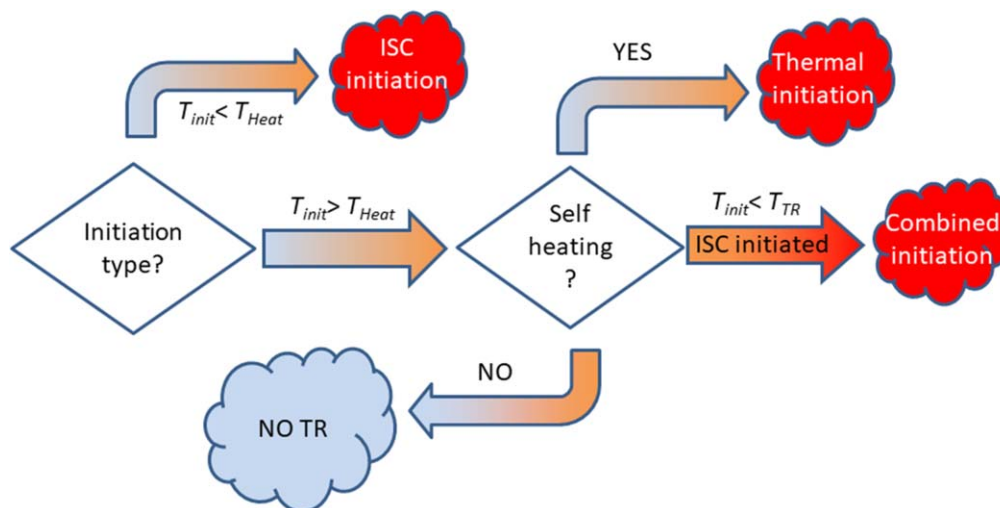| Symbol	Invariant name	Formula	Description	Dimension	Mid value	Value low	Value high	References
H_{el}	h_el	$\frac{y^0_{EL} h_{EL}}{c_p}$	Heat of reaction invariant of EL decomposition by cell weight	K	1.87×10^1	1.38×10^1	2.51×10^1	
$\mathbf{y^0_{EL}}$	—	y^0_{EL}	Initial weight percent of Electrolyte (EC)	%	0.1			This work
h_{el}	—	h_{el}	Heat of reaction of EL decomposition by EC weight	J kg^{-1}	1.55×10^5	1.40×10^5	1.71×10^5	22
E_{eva}	E_eva	E_{eva}	Activation energy - Evaporation	J	1.58×10^{19}	1.42×10^{19}	1.74×10^{19}	22
A_{eva}	A_eva	A_{eva}	Frequency factor EL evaporation	s^{-1}	2.23×10^7	2.01×10^7	2.45×10^7	22
H_{Eva}	h_eva	$\frac{y^0_{EL} h_{eva}}{c_p}$	Heat of reaction invariant of EL Evaporation by cell weight	K	-7.53×10^1	-1.01×10^2	-5.54×10^1	
h_{eva}	—	h_{eva}	Heat of reaction of EL Evaporation by EC weight	J kg^{-1}	-6.25×10^5	-6.88×10^5	-5.63×10^5	22
E_{com}	E_com	E_{com}	Activation energy—electrolyte Combustion	J	2.10×10^{19}	1.89×10^{19}	2.31×10^{19}	22
A_{com}	A_com	A_{com}	Frequency factor electrolyte combustion	s^{-1}	5.14×10^{18}	4.63×10^{18}	5.65×10^{18}	22
H_{com}	h_com	$\frac{y^0_{EL} h_{com}}{c_p}$	Heat of reaction invariant of EL Combustion by cell weight	K	2.41×10^3	1.77×10^3	3.24×10^3	
h_{com}	—	h_{com}	Heat of reaction—electrolyte combustion	J kg^{-1}	2.0×10^7	1.87×10^7	2.20×10^7	22
k_B	kb	k_B	Boltzmann constant	J K^{-1}	1.38×10^{-23}	—	—	
—	ba	$\frac{\alpha F}{RT}$	Pre exponential invariant of charge transfer reaction	—	19.34	—	—	
R	—	R	universal gas constant	J mol^{-1} K^{-1}	8.314	—	—	
α	—	α	Symmetry factor	—	0.5	—	—	
F	—	F	Faraday constant	C mol^{-1}	96500	—	—	
Δ_{init}	HHR	—	Heating rate of the heater	Ks^{-1}	1/6	—	—	

Figure 2. Flowchart of initiation strategies.

1. The simplification by a lumped model does not take into account the gradient of temperature in the battery cell. This gradient can be important due to the low conductivity of the battery cell in the thickness and radial directions for the prismatic and the cylindrical battery cells respectively. Furthermore, the description of this gradient is important for the design of an efficient battery thermal management system, especially when the design of the cooling system is included in the model.

2. Neglecting the time dependence of heat capacity and thermal conductivity is satisfactory for sensitivity analysis. They are varied in a broad range hence the importance and significance can be assessed. However, for e.g. development of protection and mitigation strategies time dependence, similar to spatial variation (limitation point 1), needs to be taken into account

3. The simplified electric model is more accurate until 30% DoD. Later on the Joule heating may be overestimated by the model

4. Thermal decomposition reactions are limited to 600 °C, and no combustion with external oxygen is considered. There may be other reactions at higher than 600 °C such as melting of current collectors (endothermic) or thermite type reactions (exothermic)

5. Reactions outside the battery cell are not modelled. Therefore, heat from combustion of vented gases with external oxygen or from decomposition of vented electrolyte e.g. in a calorimeter chamber, may need to be taken into account for specific scenarios.

6. As the temperature increases the separator initial damage may spread to other areas and therefore the initial short circuit resistance varies (decreases). All soft short may develop to hard short.

Calculation of input invariants and validation of initial parameters.—The input parameters are estimated from specific parameters of a Graphite—NMC(111) battery produced by CustomCells and intensively studied in our previous works.[22,34,46] Then their variation is calculated from the standard error of measurement (mainly from Refs. 22 and 34). When no standard error was available 10% relative error has been assumed. The design parameter of the cell (e.g. Ah loading, volume to surface ratio) and the initiation parameters are varied in broader but still in realistic ranges. Physical constants and basic material properties are not varied (character "-" shows the fixed inputs). Additionally, the tunneling effect in Eq. 26 is not varied in this work, because of model stability issues. Since the heater is considered as a perfect heater, the heating

rate is not varied either. It must be noted that by using a more stable model the sensitivity of the non-varied parameters needs to be evaluated to minimize the risk of missing an important interaction.

The ODE system was solved by Matlab's stiff ode23s solver with max step size 1 s. The input parameter combinations are generated by JMP's (SAS, USA) Latin-Hypercube algorithm. The K-Means clustering, principal component analysis and random forest predictor screening are performed by JMP. The Sobol' indices have been determined by JRC developed algorithm (https://ec.europa.eu/jrc/en/samo) based on chaos expansion.[41] The multi-nominal logistic regressions are fitted by maximum likelihood algorithm of JMP.

The output time series have been saved with 0.2 s resolution. A summary data file has been also generated summarizing the invariants used for the TR event with the calculated features of the time series. All data file can be downloaded from the supplementary materials (available online at stacks.iop.org/JES/167/090555/mmedia) for further analysis. Because of the large number of input and output data not all invariants and features are included in the text but all data can be retrieved from the attached supplementary data sets (http://doi.org/10.17632/9cykcc3svn.2).

The model parameters have been validated in two steps. First the short circuit part and second the thermal decomposition part. The aim of the validation steps is not the achievement of a perfect fit, but to demonstrate a realistic mid value around which the invariants can be varied.

Figure 3 shows the current and potential as a function of time in a semi-logarithmic scale at different resistance ratios for the experiment and the simulation. For the short circuit model the diffusion limited current invariant, j_D has been adjusted manually (increased from 0.4 to 0.635) to match the plateaus of the experimental data. Even though the simulation is not a perfect match it reflects the two main plateaus: their current rates and durations until ca. 20% of DoD. Later on, other phenomena also occur in experiments, such as venting, thermal decomposition, which is not reflected in the ECM.

Figure 4 summarizes the heat flow during anode and cathode decompositions. The experimental data of Differential Rate Calorimetry (DSC) are taken from Ref. 22. The simulated mid values (reference simulation) and several further combinations of parameters within the range covered in the simulation (see Table I) are also overlaid with the experimental DSC data. Even though the parameters are varied within the measured standard deviation, the heat flow varies over a broad range of temperature and amplitude. The variation of the activation energies changes the position of the peaks in temperature (corresponding to an anode or cathode decomposition reaction) and sometime creates overlapping peaks

(a)   (b)
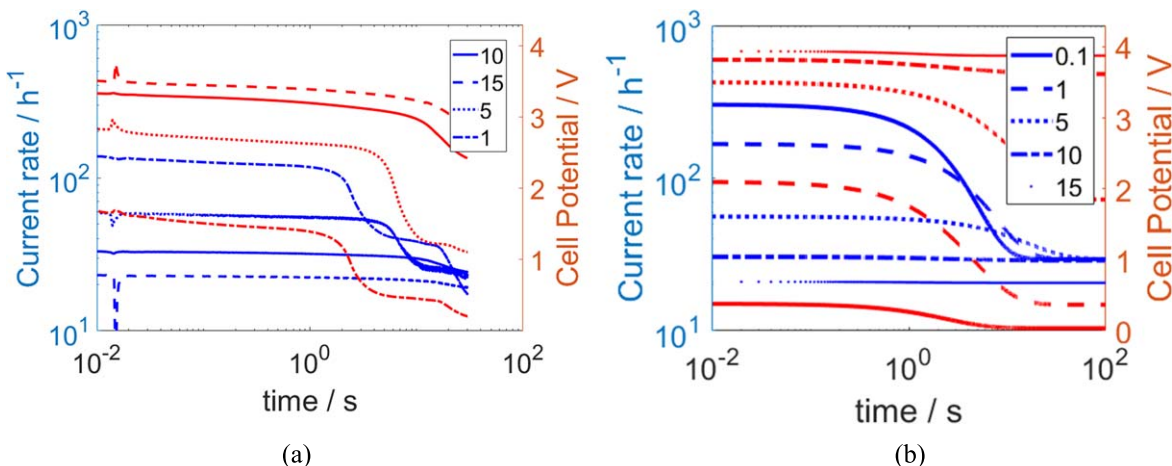
Figure 3. Experimental data from Ref. 46 (a) and the simulated (b) current (blue) and potential (red) results of external short circuit of Gr-NMC pouch cells at 5 different resistance ratios without thermal decomposition based on the model developed in this work.

(a)   (b)
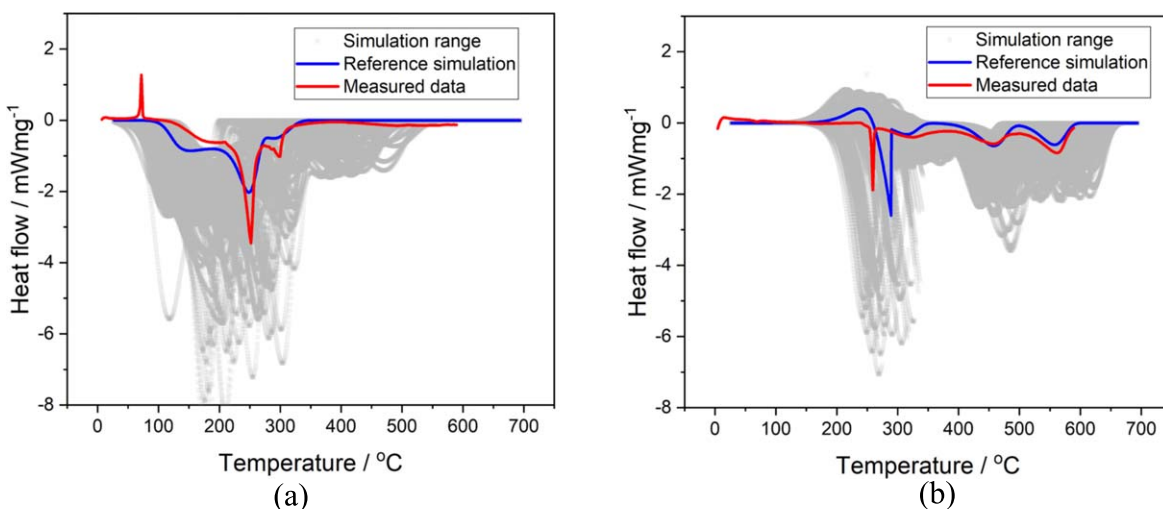
Figure 4. The simulated heat flow in the varied simulation range compared with the simulation based on mid values (reference simulation) and the experimental results from Ref. 22 for the LiC_6 (a) and NMC (b). The heating rate is 10 K min^{-1}.

in which cases the heat flows are added together resulting in sharp and high peaks. Nevertheless, the experimental data is positioned in the middle of the simulated TR events.

Results

The mid values from Table I and resistance ratio (Re) equals to 0.1 are used for the simulation of the reference scenario. The temperature evolution of TR and the decompositions of each components without any additional heating during initiation are shown in Figs. 5a and 5b, respectively. For few seconds after the initiation the short circuit current heats up the cell quickly, as it is expected from Fig. 3. Then the initial short circuit current drops to almost 1/10 but it is still high enough to continue to heat up the cell considerably. Simultaneously, the amount of lithiated graphite (LiC_6), and NMC (1 and 3 reactions) decreases proportionally with the current as the cell discharges. The anode binder and the cathode binder ratio do not change. After the temperature reaches the first break down temperature of the primary SEI, the drop of LiC_6 concentration (LiC_6) intensifies as the formation of the secondary SEI consumes LiC_6. When the second break down occurs the LiC_6 concentration reaches zero and the ISC current stops. Since the temperature is high enough the anode binder and the NMC 1 continue to decompose. In parallel with the NMC 1 decomposition oxygen is liberated, which burns the electrolyte. The negative value

of combusted and evaporated electrolyte represents the released gaseous phases which are not involved in any reactions. Simultaneously, the amount of electrolyte decays to zero and the combustion stops. Because of electrolyte evaporation and combustion consume all the electrolyte, the decomposition of the electrolyte (solvent $LiPF_6$ reaction) cannot happen. The cooling is powerful and the temperature of the cell does not reach the decomposition temperature of cathode binder and NMC 3, therefore the cell starts to cool down and the decomposition of NMC 1 and anode binder stop either.

A latin-hypercube design was chosen to define 780 different TR events. The invariants were set to evenly fill out the 39 dimensional parameter space defined by the low and high values of the invariants in Table I. The number of points is a trade-off between the resolution of the data and the computational cost. Lower resolution would result in lower statistical power and consequently smaller number of TR behaviour could be identified. Higher resolution may allow to classify more clusters and to determine the probability of TR with higher confidence, but does not change the classification of the events at lower resolution.

The temperature evolution of each TR scenario is shown in Fig. 6a. From these curves the maximum TR temperature (°C) and the temperature increase generated by the heater (°C) (i.e. maximum heating energy normalized by the heat capacity and the mass of the cell) are calculated and analysed as a function of the initiation
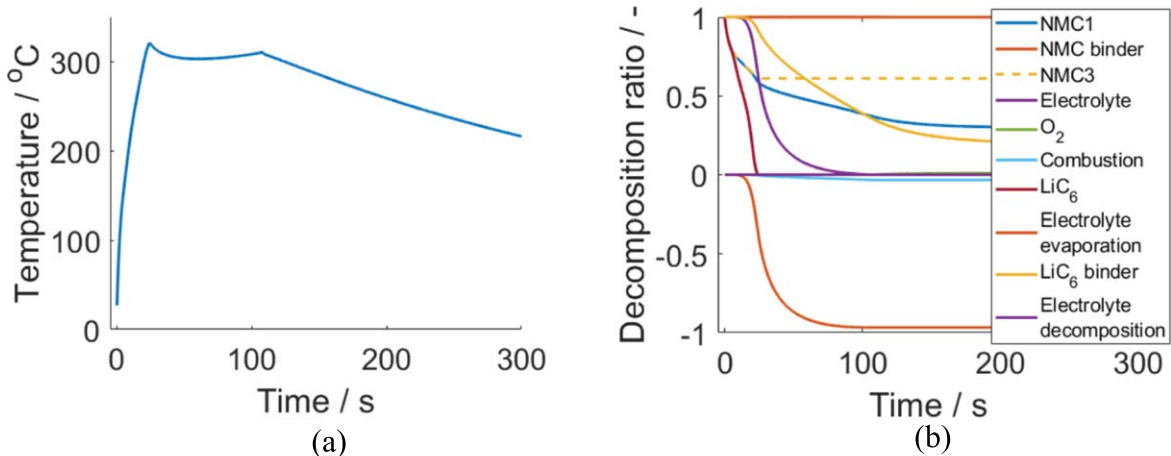
Figure 5. Simulated TR of the reference scenario with resistance ratio 0.1 when ISC happens at room temperature (i.e. TheaT = TiniT = 300 K), without additional heating. The temperature of the cell (a) and the decomposition ratio of the materials (b).
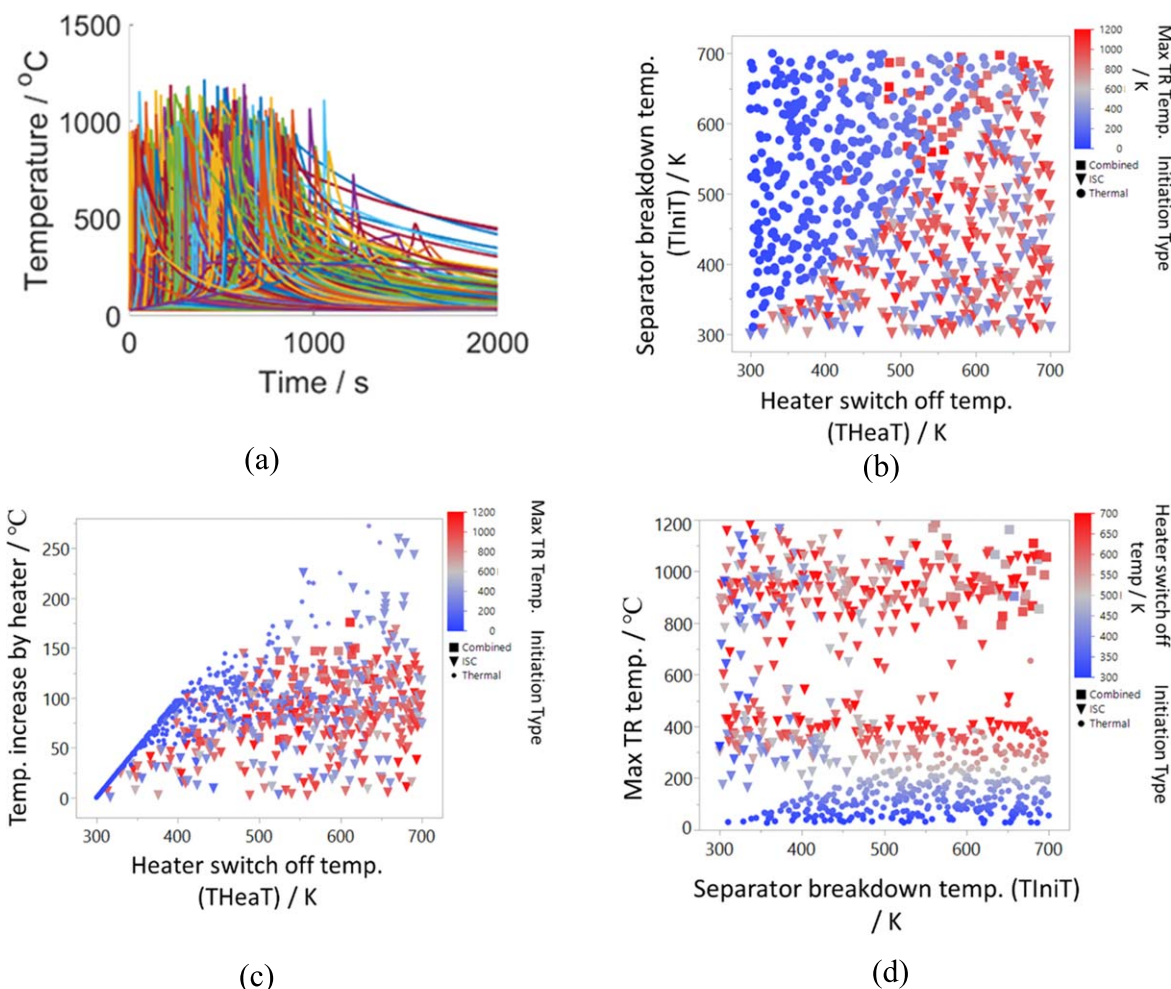

Figure 6. Visualization of the 780 TR scenarios as a function of the main initiation parameters: the time-series of TR temperature variation during TR (a), heater switch off temperature and separator break down temperature (b), heater switch off temperature and the actual temperature increase originated from the heating, (c), separator breakdown temperature and the maximum TR temperature (d) The triangle, circle and square represents ISC, thermal and combined initiation events, respectively.

parameters: heater switch off temperature, THeaT (K) and the separator breakdown temperature, TIniT (K).

In the later parts of this manuscript only the invariant names in Table I are used. This name refers to the variables in the attached data file.

Figure 6b shows the distribution of the two main initiation parameters, TIniT and THeaT. The dots are the thermally initiated events (THeaT < TIniT) and the triangles are the ISC initiated ones (THeaT > TIniT). The events depicted by squares are the combined events when the separator breakdown temperature is reached
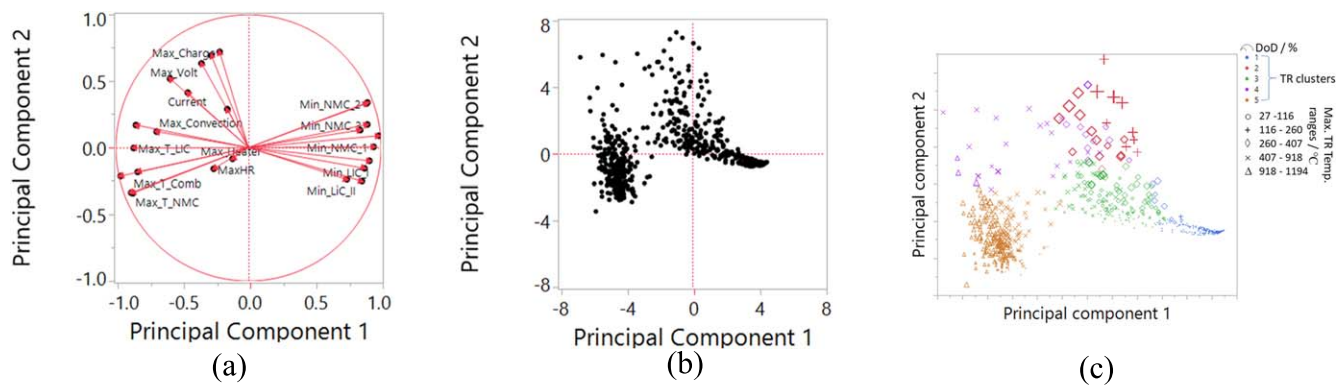
Figure 7. Principal component analysis of the features of each (780) TR events. The composition of the principal components (a) the biplot of events (b) and the result of the K-Means Clustering plotted in the first 2 principal components' coordinate system (c).

because of self-heating, despite THeaT < TIniT. Combined events happen in the upper right corner of the graph only. The colour of the points reflects the maximum TR temperature. More red points are in the lower triangle (the ISC region) than in the upper part (thermally initiated region). It may indicate that ISC induced TR may create severe TR more frequently at any triggering energy input.

Figure 6c depicts the final temperature increase (°C) generated by the heater (i.e. triggering energy) as a function of the heater switch off temperature (THeaT). The colour of the dots represents the maximum temperature during TR. The temperature increase by the heater (i.e. triggering energy) is smaller than one would expect from the heater switch off temperature, which indicates that temperature increase from self-heating or from ISC contribute to the heating of the cell considerably before the heater is switched off. The blue dots forming a straight (45°) line in the left bottom corner of Fig. 6c shows those events where maximum temperature of the cell is equal to the maximum temperature of the heater (i.e. no TR happened). Red points (mostly triangle) populates the whole lower right part, indicating that if ISC happens TR can happen regardless the triggering energy. Those dots which are further away from the 45° line represent events when self-heating started. Since many of them are deep blue this indicates that just self-heating is not always sufficient to trigger TR, because of cooling. Combined initiation (square) can be also found in a broad range of THeaT without any trivial correlation with the heater switch off temperature.

The relationship between the separator breakdown temperature and the maximum TR temperature depicted in Fig. 6d shows a complex pattern. The triangle-shape group, populated with blue dots in the bottom, consists of events without TR and without separator breakdown, i.e. thermal initiation. Two horizontal red groups are visible with an average of 400 °C and 600 °C, respectively. The combined TR events when the separator breakdown temperature is reached by self-heating of the cell, appear in the upper right corner (square). The temperature increase caused by the heater (i.e. triggering energy input) looks to have less influence on the maximum temperature for ISC initiated case because both red and blue triangles can be found in the high and low TR temperature regions. Consequently, the effect of the energy input from the heater on the maximum TR temperature, i.e. on the severity is not trivial.

Classical fitting tools cannot be applied directly for the characterization of the relationship between triggering energy and severity, because TR scenarios seem to form groups and the behaviour in the groups can be different. First, similar events are clustered and their severity is classified by using machine learning tools and then the analysis of the groups is performed separately.

Severity analysis and classification of TR events.—29 different features have been engineered for the characterization of the events from the output time series. The most significant ones are listed in Table II, the others can be found in the attached dataset. Naturally,

correlations exist between the features therefore principal component analysis has been performed and two new parameters (principal component 1 and 2) have been constructed from the linear combination of the original features (Fig. 7a). These new parameters reflect the main dimensions of the variation and can be useful to identify further patterns (Fig. 7b). Clusters have been determined by using K-means clustering. The results of K-mean clustering are plotted on a biplot of the 2 most important principal components as it is shown in Fig. 7c. where 5 different clusters are visible. The existence of clusters may indicate typical TR behaviours, in spite of that every event is different. The colour of the points represents the different clusters, the marker denotes the range of the maximum temperature during TR, while the size of the marker characterizes the internal short circuit discharge (i.e. DoD). The bottom right part of the plot represents the lowest maximum temperature with minimal discharge (DoD). The temperature toward the left increases while DoD increases toward the top. The clusters represent group of points which are close to each other in the 29 dimensional feature space and does not reflect any physico-chemical causal relationships. Therefore, the severity of the clusters is estimated by analysing cluster averages (Table II) and time-series (Fig. 8).

Figures 8b–8f depict the temperature evolution, the decomposition of LiC$_6$, NMC 1, the amount of electrolyte combustion (in the negative quarter) and the DoD. All TR events of a given cluster are plotted and few are highlighted (selected manually) which represent some characteristic behaviour. For further analysis, the time series and the engineered features can be accessed from the data repository attached to this work.
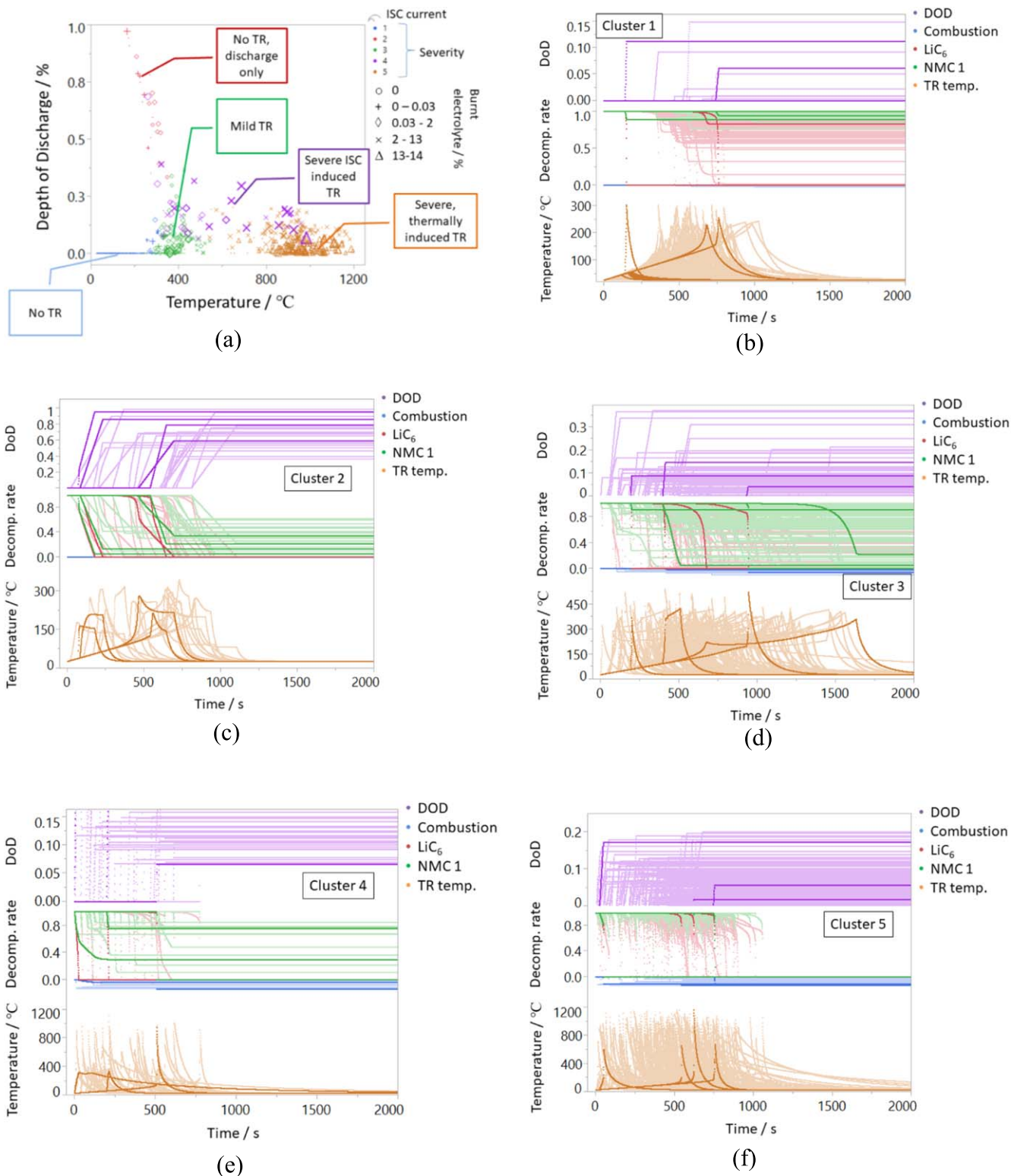
The TR scenarios of cluster 1 exhibit the lowest temperature and lowest average DoD (Table II). As Fig. 8b. depicts, this segment is dominated by the heater. The introduced feature, initiation ratio in Table II, which measures the ratio between the energy supplied by the ISC and the heater (values smaller than 1 mean that the heating of the cell originates from the heater), indicates that ISC does not happen or is not significant. Regardless of some decomposition and ISC the average maximum temperature is around 126 °C, around the onset temperature. Cluster 1 also consists of events where the cooling power is stronger than the heat generation after the onset temperature is passed or the short circuit happened. Consequently, further decomposition of the materials and TR do not take place. Cluster 1 is therefore considered as a group of thermally induced events with no TR.

Events of cluster 2 in Fig. 8c can be characterized by high DoD, small ISC current (corresponding to a soft short) and relatively low temperature. LiC$_6$ and NMC 1 fractions are reduced because of discharge and not because of thermal decomposition. Cooling can compensate the heat generation of the soft ISC. The temperature stays around 300 °C in average, therefore this group is classified to ISC induced thermal events without TR. Since DoD is higher than 20% the ECM (Fig. 1) may overestimate ISC current and ISC

Table II. The averaged properties of the different clusters determined by K-means clustering.

Severity clusters Clusters	Max. TR Temp. °C	Average of						Average final decomposition ratio of						
		Max. DoD %	Final ISC contrib. %	Final Initiation ratio	Max. Heating rate Ks^{-1}	Max. Voltage drop V	Max. Current rate h^{-1}	NMC 1 %	NMC 2 (binder) %	NMC 3 %	LiC_6 %	Anode binder %	Comb. %	Electrolyte total %
1/NO TR, NO ISC	127	0	2	0	5	0	0.7	0	0	0	12	10	0	2
2/No TR, ISC	253	68	76	15	12	1.1	39.1	70	0	68	100	18	0	42
3/Mild TR	363	5	14	1	133	0.6	20.7	34	2	5	95	47	1	85
4/Severe ISC TR	670	16	29	12	330	3	142.2	81	58	61	100	80	7	94
5/Severe TR	928	5	5	2	635	0.9	37.4	100	100	98	100	100	13	100

Figure 8. The classification of the 780 TR scenarios (a) and their time profiles (b)–(f).

heating, however it does not change the classification of the cluster (i.e. no TR).

In Cluster 3 the anode decomposes fully but only 40% of NMC 1 decomposes on average, consequently TR happens but the temperature stays below 600 °C. This cluster can be classified as mild/partial thermal runaway conditions mostly activated by the heater. Depending on the cooling power, this cluster may show the longest

TR durations as it can be seen in Fig. 8d. Since DoD remains below 20%, the application of ECM (Fig. 1) is still satisfactory.

Cluster 4 in Fig. 8e represents hard internal short conditions with total decomposition of anode and full or partial decomposition of NMC with oxygen generation and electrolyte combustion. The cooling rate cannot compensate the Joule heating caused by hard ISC. Therefore, the temperature can reach 1000 °C representing

Table III. Significant differences in the input invariants by clusters. Bold in red and italic in yellow number represent strong and weak significance level, respectively.

Severity Clusters	Re Resistance ratio	Ri Internal resistance	aa Apparent exchange current density	Ah Cell capacity	HeaT Heater cut-off temp.	IniT Separator breakdown temp.	h_conv Heat convection	h_LiC_I Reaction heat of first breakdown of LiC$_6$ (SEI)	E_LiC_II Activation energy of 2nd breakdown of LiC$_6$.	A_bin Frequency factor of 2nd breakdown of LiC$_6$	E_1 Activation energy of 1st NMC .	E_eva Activation energy evaporation of EL	A_eva Frequency factor of evaporation of EL
		$\Omega\times(As)^{-1}$	s^{-1}	$K\times V^{-1}$	°C	°C	s^{-1}	K	J	s^{-1}	J	J	s^{-1}
Multiplier		10^2	10^{-1}	10^2			10^{-2}	100	10^{-19}	10^6	10^{-19}	10^{-19}	10^7
1 / NO TR	5.1	1.1	1.08	2.9	**126**	269	1.2	3.1	2.7	5.7	2.4	1.6	2.23
2 / No TR, ISC	5.8	1.3	*1.12*	**1.95**	*201*	**127**	**1.6**	2.8	**2.9**	*4.5*	2.4	1.6	2.28
3 / Mild TR	5.5	1.2	1.08	3	306	241	1.1	3.1	2.6	5.6	**2.5**	**1.5**	*2.25*
4 / Severe ISC TR	**1.9**	*0.7*	*1.0*	2.72	*271*	**83**	1.1	2.9	2.7	5.7	2.4	1.6	*2.18*
5 / Severe TR	5.2	1.2	1.09	2.96	300	199	1.1	*3.5*	2.7	5.6	**2.2**	1.6	2.23

severe TR conditions. Regardless of the hard short, the DoD is 16% because the decomposition reaction also consumes active materials. The feature ISC contribution (Table II) defines the ratio of the heat generated by ISC and by thermal decomposition. The contribution of ISC to the heat generation during TR is 29% in average which is close to the estimation of Coman[16] in their hard ISC test and simulation.

Cluster 5 consists of the most severe TR scenarios as it is shown in Fig. 8f. The temperature reaches over 1000 °C, the highest fraction of electrolyte is combusted, and full decomposition of all active materials occur. Initiation ratio (ISC heating/Heater heating) is low therefore mostly thermal initiation occurs in this cluster.

The most distinctive differences between the clusters are: maximum TR temperature, DoD, short circuit current (current rate) and the amount of combusted electrolyte. Figure 8a summarizes the correlations among the clusters and the proposed classification. The max temperature and decomposed active material ratio, correlates with the amount of burned electrolyte. If less than 1% of electrolyte is combusted with the generated oxygen from the NMC, the maximum temperature remains lower than 600 °C. In spite of the amount of burned electrolyte is small (<2%) it can add enough energy to the system which activates the decomposition of NMC 2 (cathode binder) and NMC 3 which brings the maximum TR temperature well above 800 °C.

The next subsection studies the sensitivity of the output on input invariants. Two main analyses are performed: 1) identification of the significant input invariants by using Analysis of Variance (ANOVA) and 2) quantification of the sensitivity as follows. First an invariant screening method is used and the most influential invariants are selected for further analysis. Then a multi-nominal logistic fit is applied and the probability of the occurrence of the different TR clusters is determined as a function of the most influential invariants. It must be noted that this probability characterizes the effect of all other invariants and cannot be directly translated to the probability of TR of a concrete cell.

Sensitivity analysis between clusters.—Analysis of variance (ANOVA) is applied to study the significant differences of the input invariants between the TR severity clusters. Table III shows the cluster averages of 13 input invariants for each of the 5 clusters. The text with red, orange and black indicates high, moderate and no or low significance in the difference between the cluster averages. The non-listed invariants do not show any significant differences between the clusters, but this does not mean that they are not important. It only means that their variation in the selected range is not significant regarding the chosen classification of TR. Therefore, their average can be used, which in turn reduces the complexity of the simulation problem.

Table III clearly demonstrates that there is no global invariant which would explain the behaviour of the system. Consequently, separate analysis of the clusters may give more meaningful results than global analysis (i.e. fitting).

In cluster 1 (thermal activation without TR) the only significant difference is the low heating temperature (TheaT) or in other words

small energy input to the system (Table III). The separator breakdown temperature (TInit) is higher than the heating temperature, which explains why no or very small electric discharge occurs as it is indicated in Table II.

Cluster 2 represents those cases when ISC happens but no TR occurs since the maximum average temperature of TR is below 300 °C as it is shown in Table II. Table III shows, that this cluster is represented by soft ISC, low charge density or high heat capacity cells and intense heat convection (h_conv). ISC is triggered before the heater switches off. The heat convection invariant is the highest among all clusters, which is important to stop severe overheating and TR. The high activation energy of the second break down of the anode can be an important factor to avoid TR. Interestingly, reaction heats do not appear to be significant invariants but the activation energy and frequency factor do. If the heat generation rate is higher than the heat dissipation rate at the beginning of TR, this increases the chance that the system reaches the decomposition of the NMC and consequently a more severe TR develops. Therefore, keeping the activation energy high might be more important than to keep the overall heat generation low.

Mild TR by thermal activation (cluster 3) happens if the activation energy of NMC 1 is high and the electrolyte evaporation activation energy is low. It represents cases when all electrolyte evaporates before oxygen is generated from NMC 1 decomposition.

The main characteristics of cluster 4 (severe TR with ISC) are the low resistance ratio, low internal resistance of the cell and low separator break-down temperature. This also means that any cell with hard internal short may develop to severe TR.

Severe TR by thermal initiation (cluster 5) can be characterized by high rate of electrolyte combustion. However, none of the thermal triplets of the electrolyte burning reaction are significantly different in cluster 5, but the activation energy of the first decomposition of the NMC (NMC 1) is. If the decomposition of NMC 1 starts at lower temperature (i.e. smaller activation energy), more oxygen is generated resulting in higher amount of electrolyte combustion which in turn creates a more severe TR.

The found differences are in line with the classification of the clusters.

Calculation of probability of TR severity.—In this sub section the quantification of the sensitivity is performed. Sobol' indices are calculated by using chaos expansion algorithm developed by JRC[41] and are used to screen the most significant invariants and their interactions. Random forest based screening (by JMP) is also applied as further confirmation for sensitive invariants. Then the effects are visualized by using multi-nominal logistic regression.

The Sobol' indices and the random forest predictor screening resulted in the same invariants but with slightly different ranking, therefore only the Sobol's result is shown in Table IV. The invariants in Tables III and IV highly overlap, which supports the classification introduced previously. The heater switch-off temperature (i.e. the triggering energy) is the most influential which is expected because for thermally initiated TR the onset temperature is

Table IV. Sensitivity between the severity clusters, ranked by Sobol' indices. Interaction between two invariants are shown by two names in the column separated by '&'.

Invariants	THeaT	TIniT	E_1	THeaT&TIniT	THeaT&E_1	E_Eva	Ah	Re	Ah&TIniT	h_LIC_I	Ri	h_LIC_II	h_conv
Sobol' Indices	0.47	0.28	0.14	0.08	0.07	0.03	0.03	0.03	0.02	0.02	0.02	0.02	0.01

needed to be exceeded to trigger TR. The separator breakdown temperature (TIniT) is less expected to be an influential invariant. The reason for its possible importance is discussed later. It is also important to note that only the anode decomposition heat is influential on the severity and not the cathode or electrolyte decomposition heats. It may indicate that more heat generation in the beginning of TR can increase the cell's temperature faster and therefore enables the decomposition of all materials. Therefore, the reaction heats at later stages do not have influential role in the severity. Although, they influence the maximum temperature and the overall heat generation. The resistance ratio (Re) and the activation energies of NMC decomposition and electrolyte evaporation are also influential on the severity of TR. Hard ISC creates powerful Joule heating in the beginning which similarly to the previous scenario brings the cell's temperature to the onset of the decomposition processes. The activation energies influence the combustion of electrolyte which in turn influence the severity of the event.

In the following we quantify the effect of the influential invariants (Table IV) by estimating the probability of the different TR clusters by using nominal logistic regression. It is assumed that the odds of a TR event has a binomial distribution as follows:

$$\frac{1}{(1 + \exp(\text{Odds}(\xi)))} \quad [34]$$

where the Odds is the ratio of the probability of TR and NO TR (or other categorical variables), which is approximated by a first order function of invariants:

$$\text{Odds} = C + \sum_i \alpha_i \xi_i + \sum_i \sum_{j \neq i} \beta_{i,j} \xi_i \xi_j \quad [35]$$

where C, α_i, $\beta_{i,j}$ are predictors of the intercept, the main effects and the interactions, respectively. ξ_i and ξ_j are different invariants from Table I.

Because of the large number of invariants, the fitting algorithm may not be convergent. Therefore, to facilitate convergence only the screened invariants in Table IV are used in the regression. In the final model the number of the invariants and their interactions are narrowed down only to the statistically significant invariants to avoid overfitting and to reduce the complexity. Even the simpler model contains several interactions, therefore the multidimensional dependency of the invariants on TR severity clusters are explained from simple to complex cases as follows:

1. estimation of the probability of TR for all events,
2. estimation of the probability of severe TR when TR occurs,
3. estimation of the probability of all severity clusters for ISC initiated events. The probability of the severity is analysed separately for hard and soft ISC.
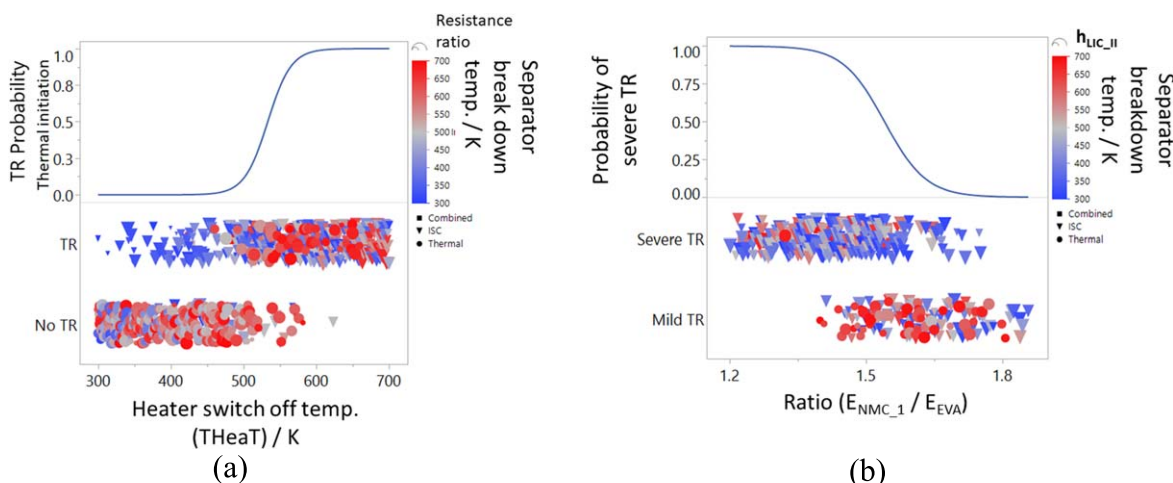
The invariants name from Table I is used in the following and not their symbols, because it can be easier to interpret and reuse the attached datasets. (http://doi.org/10.17632/9cykcc3svn.2)

Estimation of the probability of TR for all events.—Figure 9a shows the estimated probability of TR. It is assumed that TR occurs in clusters 3, 4 and 5, while cluster 1 and 2 do not result in TR. The screening showed that THeaT and TIniT are the most influential invariants for determining if the cell goes to TR or not. During the fitting process both invariants and their interaction were found to be significant. The lower part of Fig. 9a represents each TR event grouped by TR and NO TR classes as a function of the heater switch off temperature (THeaT). The colour of the points shows the separator breakdown temperature. The type of marker such as square, dot and triangle represent combined, thermal and ISC initiation, respectively. The upper part (continuous line) is the calculated probability of TR for only thermal initiation (TIniT = 700 K). The probability curve shows that thermally initiated TR happens only above ca. 550 K (277 °C), which is the reference temperature of the second breakdown of the SEI at the anode. However, TR happens at any temperature if it is initiated by ISC because the triangles are distributed evenly. TR initiation is analysed later in more details.

Estimation of the probability of severe TR when TR occurs.—When TR happens it can be mild or severe. Clusters 4 and 5 (ISC and thermal initiation) are classified as severe TR and cluster 3 as mild TR. Figure 9b shows the events grouped by severe and mild TR and the probability of severe TR as a function of the activation energy ratio at reference (mid) values (Re = 1, h_LIC_II = 108 and IniT = 450 K). The most significant invariants are: the activation energy of NMC 1 (E_1), electrolyte evaporation (E_eva), resistance ratio (Re), reaction heat of secondary break down (h_LIC_II) and the separator break-down temperature (IniT). No significant interaction between E_1 and E_eva is found, therefore a new invariant is introduced as the ratio of the activation energies (E_1/E_eva). Weaker interaction found between ITniT and E_eva and between IniT and h_LiC_II, but this is not investigated further in this work. When the activation energies of NMC 1 (E_1) and electrolyte evaporation (E_eva) are close (ratio close to 1) electrolyte burns and severe TR happens. When the electrolyte evaporates before the decomposition of NMC (the ratio is close to 2), mild TR happens. If the ratio is in between, hard ISC and the reaction heat of the second breakdown of the SEI (h_LIC_II) can increase the probability of severe TR. More blue points in severe TR indicates that lower separator breakdown temperature increases the probability of severe TR. More small points are present in the mild TR indicating that smaller reaction heat of the secondary SEI break-down increases the chance for mild TR.

(a)   (b)

Figure 9. Probability of TR at TIniT = 700 °C (a) and severe TR when TR happened (b) as a function of the most significant invariants.

Estimation of the probability of severity clusters for ISC initiated events.—Manufacturing faults create TR by ISC. Mathematically it means those TR events when TIniT < THeaT. Ideally further energy input (e.g. heating) should be stopped when the separator breaks down, however in real initiation experiments an immediate switch-off of the heater can be hardly realized, therefore the effect of additional heating energy is also analysed separately before and after ISC is triggered. The most significant effects of the invariants on the severity of TR is screened by Sobol' indices and random forest before. Then a multi-nominal logistic regression is applied by using the screened invariants only (Table IV) but by taking into account the interactions between them. The outcome is a simplified descriptive model of the simulation results, but according to the confusion matrix in Table V the accuracy is still acceptable. In total 16% of the events are classified wrongly and the failed predictions are mostly between mild and severe TR.

The outcome of the regression, i.e. the probability of TR severity clusters is used to visualize uncertainty and sensitivity. Figures 10–12 contain a graph for each significant invariant depicting the sensitivity of the given invariant. All graphs plot the cumulative probability of all severity classes. The black lines divide the plots of each invariant into several areas. A number is shown in each closed area, corresponding to a severity cluster. The red vertical and horizontal dotted lines denote the actual value of the invariant and the probability of the clusters, respectively. If the value of an invariant varies all the other black lines vary (interaction between the invariants are considered) and the probability of the clusters also varies. Therefore, this coupled variation is presented for three different invariant combinations. Between the selected cases the resistance ratio (Re) and the ratio between the activation energy of NMC decomposition and electrolyte evaporation are varied. It must be noted that the presented cases are just a snapshot of the very complex behaviour of TR.

Table V. Confusion matrix of the multi-logistic regression on the severity of TR. The diagonal is the correctly classified while the upper and lower triangles are the falsely classified by the simplified model.

| Actual severity	Predicted severity			
	2	3	4	5
2	**13**	3	1	4
3	2	**80**	3	16
4	1	2	**27**	4
5	3	11	3	**196**

Figure 10 shows the significant invariants when the electrolyte burning ratio is low (i.e. the electrolyte combustion is significant). This scenario is similar to Fig. 9 and it shows that when the electrolyte is not evaporated until the oxygen liberation from NMC starts, TR is the most severe (severity level 5) and is independent from any other invariants.

At moderate electrolyte combustion hard ISC results in severity level 4 as it is shown in Fig. 11. The most influential invariants are the resistance ratio, the internal electrical resistance of the cell and the heat convection invariant. High internal resistance or/and fast heat convection create less severe events (cluster 2), which is expected from the physical processes. Cell design may also change the severity of TR: high Ah capacity cells tend to create more severe TR, than low Ah capacity cells. It must be noted that the invariant Ah is the ratio of the cell's Ah and heat capacity.

The heating rate of hard ISC is much higher than the heating rate of the heater therefore additional heating energy after the ISC is triggered does not influence the severity considerably. However,
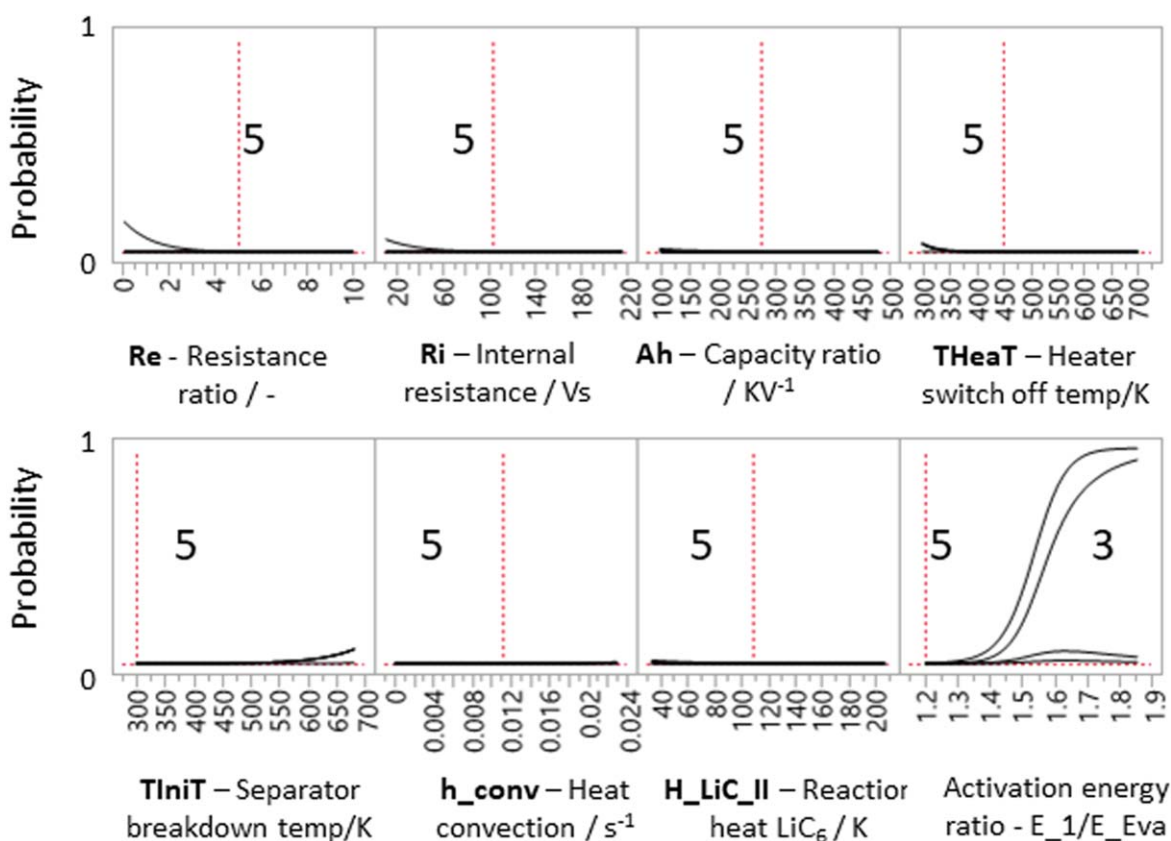
Figure 10. Effect of electrolyte combustion on TR severity clusters for ISC triggered events (TIniT < THeaT). The numbers in the areas are the severity level of the event. The red lines are the invariants value in the above example.
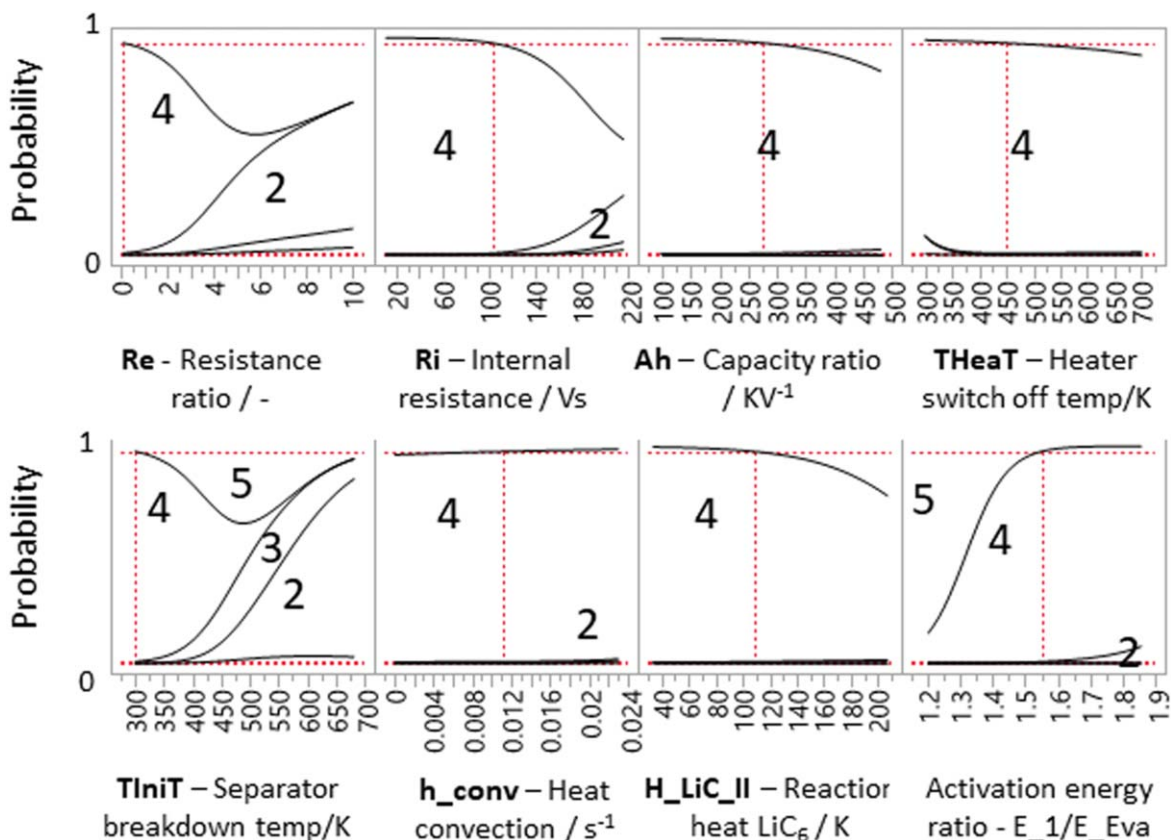
Figure 11. Effect of resistance ratio on the probability of TR severity for ISC triggered events. The numbers in the areas are the severity level of the event. The vertical red lines are the invariants value and the horizontal red lines are the probability ratios in the above example.

higher heater switch off temperature makes the heat convection invariant less influential (this case is shown in Fig. 11). On the other hand, the variation of the separator breakdown temperature, i.e. triggering energy until ISC, has influential effect on the severity and on the uncertainty. At low TIniT temperatures severity cluster 4 occurs, but at high TIniT temperatures (it also needs higher THeaT) mild TR (cluster 3) to severe (5) can occur also. This is the result of two competing processes: 1) indirect effect of heating which blocks cooling therefore increases the probability of cluster 5, 2) consumption of active materials and evaporation of electrolyte take place during the slow heating which reduces the energy content of the cell. Therefore, the uncertainty of TR severity increases if the initiation method needs more heating to initiate ISC.

The severity of the initiation at soft ISC varies more than at hard ISC. Cell chemistry and cell design parameters such as reaction heat of decomposition, Ah capacity become more influential than at hard ISC. The severity is very sensitive to the heater switch off temperature or in other words the triggering energy, and also to the separator breakdown temperature. More triggering energy input until ISC brings the cell from mild to severe TR (from 3 to 5). On the other hand, the increase of the separator breakdown temperature reduces severity. Therefore, the triggering energy both before and after the ISC has much higher influence on the severity than in the case of hard ISC. Consequently, a very precise control of the initiation parameters at soft ISC is needed to reach a repeatable and reproducible test, which can be more challenging than at hard ISC.

Discussion

The selection of a repeatable, reproducible, fit-for-purpose and technology agnostic initiation condition is not an easy task. Furthermore, a test should not limit innovation and the development of intrinsically safer solutions, but should reduce the possibility of manipulation of the outcome. In the following we discuss the pro-cons of different initiation conditions based on the results of the simulation.

In this work we showed that 5 different severity clusters are distinguishable despite the 39 continuous invariants, among which 8 was found to be the most significant on the severity clusters. They may be grouped to:

1. Initiation parameters: Heater cut off temperature (THeaT), Separator breakdown temperature (TIniT), Resistance ratio (Re)
2. System/cell design parameters: Ratio of Ah capacity and heat capacity (Ah), heat convection (h_conv), internal resistance (Ri) invariant
3. Chemistry related parameters: heat of reaction of secondary breakdown of the anode (h_LiC_II), activation energy of NMC (E_1) and electrolyte evaporation (E_eva).

Group 2 and 3 are under the control of the manufacturer. More thermally energetic chemistries (characterized by group 3) may be mitigated by appropriate system design e.g. parameters in group 2. If the system is thermally unstable (because of e.g. electrolyte combustion happens) as Fig. 10 shows, the test always result in the most severe TR regardless of any smart manipulation of initiation conditions or system design. Therefore, unstable cells can be excluded unambiguously.

When the combustion is not so extensive initiation parameters have influential role on the severity of TR. At soft ISC conditions the severity of TR is very sensitive to the initiation parameters (Fig. 12) hence the reproducibility and repeatability can be low. Furthermore, this condition allows more room for manipulation. On the other hand, manufacturers have more possibilities to mitigate the occurrence of severe TR or even TR. Moreover, the resistance of the soft
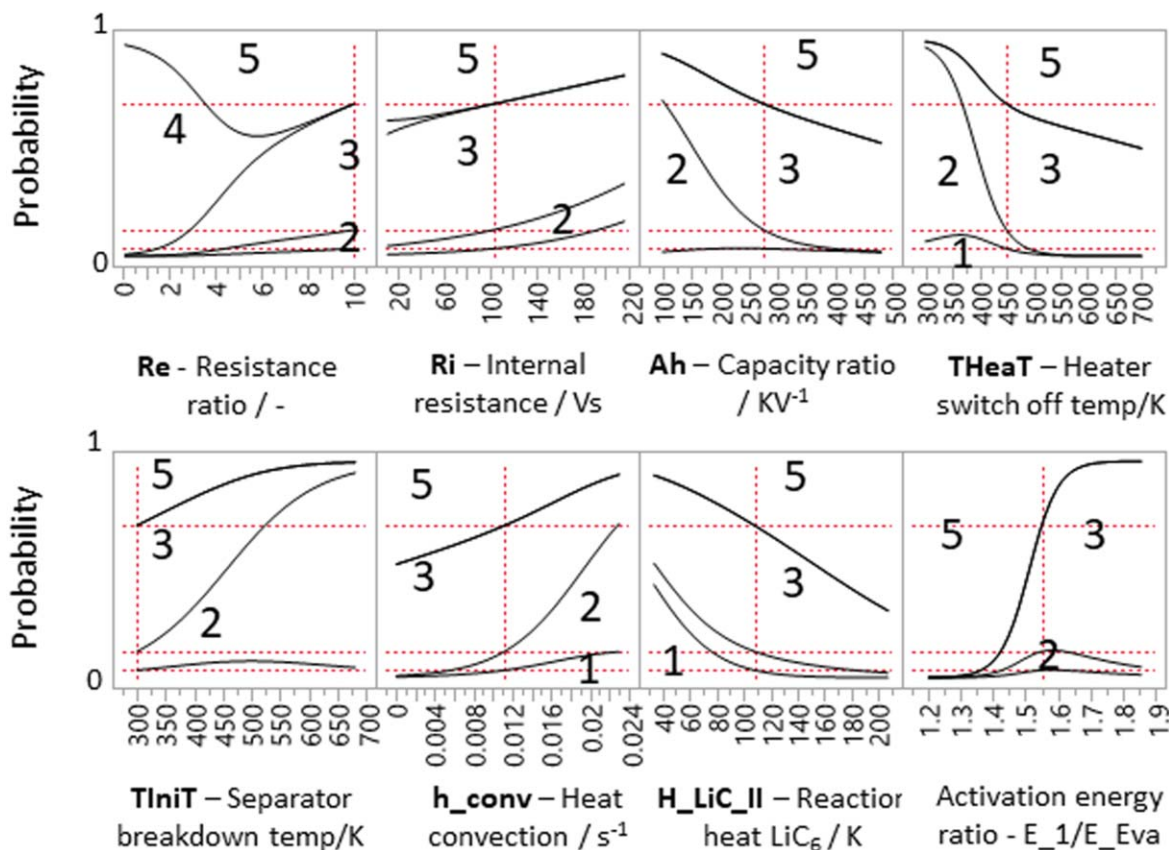
Figure 12. Effect of cell design parameters at soft short condition on the probability of TR severity for ISC triggered. The numbers in the areas are the severity level of the event. The vertical red lines are the invariants value and the horizontal red lines are the probability ratios in the above example.

ISC is very hard or maybe impossible to measure and to control which further reduces reproducibility and repeatability.

Hard ISC can be achieved with more certainty and according to Fig. 11 it is less sensitive to other parameters but still allows the application of certain design strategies to mitigate severity: for example application of forced cooling or phase change materials (which reduces invariant Ah by increasing Cp of the cell). However, ISC should happen at low temperature with small amount of energy (heat) insertion. Not because of the additional energy would have an influential impact on the severity after the ISC is triggered, but because during the heating phase the materials may decompose partially and/or evaporate resulting in reduced SOC and amount of combustible materials. Hard short at low temperature can be achieved by methods which create local damage in the separator (e.g. optimized nail penetration,[6] fast local heating method, wax method[49,50] or inductive heating[51]) without heating the full cell.

Conclusions

The main objective of the work was to understand the effect of the initiation parameters on the severity of TR. A coupled thermal-electric model has been developed which takes into account multistage decomposition reactions of active materials and interaction among oxygen liberation, electrolyte combustion, evaporation and decomposition. The initiation has been controlled by the triggering energy, the temperature where the separator beaks down and the internal short circuit resistance ratio (ratio of internal resistance and short circuit resistance).

Beside the initiation parameters all the 39 different model invariants have been varied in 780 different combinations. Despite the uniform distribution of the inputs TR events formed clusters which clusters have been classified as: (1) no TR, (2) thermal events, (3) mild TR, (4) severe TR created by ISC trigger and (5) severe TR created by thermal or combined trigger.

Sensitivity analysis on the clusters revealed that the most important parameters of both thermal and ISC triggered TR events are the triggering energy input, internal short resistance ratio, cooling power, electrolyte combustion and the heat release from anode decomposition. The heat release at higher temperature, e.g. from NMC cathode, is less influential on the severity. However, the overall energy release and the maximum TR temperature depend on the reaction heats of all materials.

The severity of TR triggered by hard internal short does not change considerably with additional energy input after ISC. However, the triggering energy input until the ISC is influential and can alter the severity of TR. Methods which create only soft ISC can be less repeatable because TR severity depends on several other parameters. The triggering energy before and after the ISC is also influential in this case: more energy input may create severe TR instead of mild TR. Therefore, methods creating hard short at low additional energy input seems to be crucial to achieve repeatable and reproducible TR initiation.

Further work on a more detailed 2D model with quasi-random low-discrepancy sequences which is more appropriate for multi-dimensional integration, hence for sensitivity analysis, is ongoing.

ORCID

Akos Kriston ⓘ https://orcid.org/0000-0003-2873-4447
Andreas Pfrang ⓘ https://orcid.org/0000-0002-6676-4893

References

1. V. Ruiz, A. Pfrang, A. Kriston, N. Omar, P. Van den Bossche, and L. Boon-Brett, *Renew. Sustain. Energy Rev.*, **81**, 1427 (2017).
2. A. Pfrang, A. Kriston, V. Ruiz, N. Lebedeva, and F. di Persio, *Safety of Rechargeable Energy Storage Systems with a focus on Li-ion Technology*, 253 (2017).
3. M. Yoshio, R. J. Brodd, and A. Kozawa, *Lithium-Ion Batteries*, ed. Y. Masaki, J. B. Ralph, and K. Akiya (Springer, New York) (2015).
4. M. Jacoby, *Chem. Eng. News*, **85**, 26 (2007), https://pubsapp.acs.org/cen/science/85/8551sci1.html.
5. V. Ruiz, L. Boon-Brett, M. Steen, and L. Van den Berghe, *Putting Science into Standards: Workshop - Summary & Outcomes. Driving Towards Decarbonisation of Transport: Safety, Performance, Second Life and Recycling of Automotive Batteries for e-Vehicles* (European Union, Petten (The Netherlands)) (2016).
6. J. Diekmann, S. Doose, S. Weber, S. Münch, W. Haselrieder, and A. Kwade, *J. Electrochem. Soc.*, **167**, 090504 (2020).
7. United Nation Economic Commission for Europe, Global Technical Regulation on Electric Car Safety (2017), http://unece.org/fileadmin/DAM/trans/doc/2017/wp29/ECE-TRANS-WP29–2017–138e.pdf.
8. ISO 6469-1:2019, Electrically propelled road vehicles—Safety specifications—Part I: Rechargeable energy storage system (RESS) (2019).
9. UL 1642, Standard for Lithium Batteries (2012).
10. V. Ruiz Ruiz and P. Andreas, *JRC Exploratory Research : Safer Li-ion Batteries by Preventing Thermal Propagation* (Publications Office of the European Union, Petten (The Netherlands)) p. 8 (2018).
11. Z. Guo, J. Zhu, J. Feng, and S. Du, *RSC Adv.*, **5**, 69514 (2015).
12. X. Liu et al., *Joule*, **2**, 2047 (2018).
13. S. Abada, G. Marlair, A. Lecocq, M. Petit, V. Sauvant-Moynot, and F. Huet, *J. Power Sources*, **306**, 178 (2016).
14. T. D. Hatchard, D. D. MacNeil, A. Basu, and J. R. Dahn, *J. Electrochem. Soc.*, **148**, A755 (2001).
15. G. H. Kim, A. Pesaran, and R. Spotnitz, *J. Power Sources*, **170**, 476 (2007).
16. P. T. Coman, E. C. Darcy, C. T. Veje, and R. E. White, *J. Electrochem. Soc.*, **164**, A587 (2017).
17. X. Feng, L. Lu, M. Ouyang, J. Li, and X. He, *Energy*, **115**, 194 (2016).
18. R. M. Spotnitz, J. Weaver, G. Yeduvaka, D. H. Doughty, and E. P. Roth, *J. Power Sources*, **163**, 1080 (2007).
19. C. F. Lopez, J. A. Jeevarajan, and P. P. Mukherjee, *J. Electrochem. Soc.*, **162**, A2163 (2015).
20. F. Larsson, J. Anderson, P. Andersson, and B.-E. Mellander, *J. Electrochem. Soc.*, **163**, A2854 (2016).
21. A. W. Golubkov, S. Scheikl, R. R. Planteu, G. Voitic, H. Wiltsche, C. Stangl, G. Fauler, A. Thaler, and V. Hacker, *RSC Adv.*, **5**, 57171 (2015).
22. A. Kriston, I. Adanouj, V. Ruiz, and A. Pfrang, *J. Power Sources*, **435**, 226774 (2019).
23. W. Q. Walker, J. J. Darst, D. P. Finegan, G. A. Bayles, K. L. Johnson, E. C. Darcy, and S. L. Rickman, *J. Power Sources*, **415**, 207 (2019).
24. S. Yayathi, W. Walker, D. Doughty, and H. Ardebili, *J. Power Sources*, **329**, 197 (2016).
25. X. Feng, J. Sun, M. Ouyang, F. Wang, X. He, L. Lu, and H. Peng, *J. Power Sources*, **275**, 261 (2015).
26. M. Zhang, J. Du, L. Liu, A. Stefanopoulou, J. Siegel, L. Lu, X. He, X. Xie, and M. Ouyang, *J. Electrochem. Soc.*, **164**, A3038 (2017).
27. F. Larsson and B.-E. Mellander, *J. Electrochem. Soc.*, **161**, A1611 (2014).
28. D. P. Finegan, M. Scheel, J. B. Robinson, B. Tjaden, M. Di Michiel, G. Hinds, D. J. L. Brett, and P. R. Shearing, *Phys. Chem. Chem. Phys.*, **18**, 30912 (2016).
29. D. Finegan et al., "Identifying the cause of rupture of Li-ion batteries during thermal runaway." **3**, 1700369 (2018).
30. A. Rheinfeld, A. Noel, J. Wilhelm, A. Kriston, A. Pfrang, and A. Jossen, *J. Electrochem. Soc.*, **165**, A3427 (2018).
31. T. G. Zavalis, M. Behm, and G. Lindbergh, *J. Electrochem. Soc.*, **159**, A848 (2012).
32. K. C. Chiu, C. H. Lin, S. F. Yeh, Y. H. Lin, and K. C. Chen, *J. Power Sources*, **251**, 254 (2014).
33. W. Zhao, G. Luo, and C. Y. Wang, *J. Electrochem. Soc.*, **162**, A207 (2015).
34. A. Rheinfeld, J. Sturm, A. Noel, J. Wilhelm, A. Kriston, A. Pfrang, and A. Jossen, *J. Electrochem. Soc.*, **166**, A151 (2019).
35. A. Hofmann, N. Uhlmann, C. Ziebert, O. Wiegand, A. Schmidt, and T. Hanemann, *Appl. Therm. Eng.*, **124**, 539 (2017).
36. X. Feng, S. Zheng, X. He, L. Wang, Y. Wang, D. Ren, and M. Ouyang, *Front. Energy Res.*, **6**, 126 (2018), https://frontiersin.org/article/10.3389/fenrg.2018.00126/full.
37. X. Feng, M. Ouyang, X. Liu, L. Lu, Y. Xia, and X. He, *Energy Storage Mater.*, **10**, 246 (2018).
38. P. Huang, H. Chen, A. Verma, Q. Wang, P. Mukherjee, and J. Sun, *J. Hazard. Mater.*, **369**, 268 (2019).
39. A. Saltelli, M. Ratto, T. Andres, F. Campolongo, J. Cariboni, D. Gatelli, M. Saisana, and S. Tarantola, *Global Sensitivity Analysis. The Primer* (John Wiley & Sons, Ltd., Chichester, United Kingdom) (2007).
40. C. Kamath, *Scientific Data Mining* (Society for Industrial and Applied Mathematics, Philadelphia) (2009).
41. Q. Shao, A. Younes, M. Fahs, and T. A. Mara, *Comput. Methods Appl. Mech. Eng.*, **318**, 474 (2017).
42. F. A. C. Viana, *Qual. Reliab. Eng. Int.*, **32**, 1975 (2016).
43. Q. Wang, P. Ping, X. Zhao, G. Chu, J. Sun, and C. Chen, *J. Power Sources*, **208**, 210 (2012).
44. K. Somasundaram, E. Birgersson, and A. S. Mujumdar, *J. Power Sources*, **203**, 84 (2012).
45. T. L. Bergman, A. S. Lavine, F. P. Incropera, and D. P. DeWitt, *Fundamentals of Heat and Mass Transfer* (Wiley-VCH Verlag GmbH & Co. KGaA, New York) 8th ed. (2011).
46. A. Kriston et al., *J. Power Sources*, **361**, 170 (2017).
47. P. M. Biesheuvel, M. van Soestbergen, and M. Z. Bazant, *Electrochim. Acta*, **54**, 4857 (2009).
48. A. A. Franco, *RSC Adv.*, **3**, 13027 (2013).
49. D. P. Finegan et al., *Energy Environ. Sci.*, **10**, 1377 (2017).
50. M. Keyser, E. Darcy, D. Long, and A. Pesaran, *Passive Safety Device and Internal Short Tested Method for Energy Storage Cells and Systems*, US pat. 9,142,829 (2010).
51. A. Kriston, A. Kersys, A. Antonelli, S. Ripplinger, S. Holmstrom, S. Trischler, H. Döring, and A. Pfrang, *J. Power Sources*, **454**, 227914 (2020).